ABSTRACT

Title of Document: EXPERIMENTAL PERFORMANCE EVALUATION OF DESORBER IN A HYBRID ABSORPTION VAPOR COMPRESSION SYSTEM

Bracha Tova Mandel, Master of Science, 2013

Directed By: Research Professor Yunho Hwang, Ph.D.
Department of Mechanical Engineering

A single-effect absorption facility was designed and constructed to experimentally investigate the performance of a 3 kW mini-channel desorber using an R134a/POE32 solution mixture. The facility was fabricated to simulate a hybrid absorption/vapor compression system for an off-grid high temperature application utilizing an air-cooled absorber. Desorber design replicated the utilization of waste heat from a generator source. The effects of temperature, pressure, solution mass flow rate and refrigerant concentration variations on desorber and desorption performance were investigated and analyzed through vapor generation, circulation ratio, poor solution concentration, desorber mean heat transfer coefficient and quality

difference. Desorber heat transfer coefficient enhancement was found to be a strong function of solution temperature, rising by up to 75% with a 30°C temperature increase. Due to poor absorber performance, increasing solution temperatures and mass flow rates did not result in a proportional desorber vapor generation enhancement, leading to a reduction in desorber quality difference.

EXPERIMENTAL PERFORMANCE EVALUATION OF DESORBER IN A HYBRID ABSORPTION VAPOR COMPRESSION SYSTEM

By

Bracha Tova Mandel

Thesis submitted to the Faculty of the Graduate School of the
University of Maryland, College Park, in partial fulfillment
of the requirements for the degree of
Master of Science
2013

Advisory Committee:
Research Professor Yunho Hwang, Chair
Professor Balakumar Balachandran
Associate Professor Bao Yang

Dedication

To Jarah

Acknowledgements

As Ralph Waldo Emerson once said: “Life is a journey, not a destination.” As such, I would like to thank all those who have made this journey a true scholastic adventure. To begin with, I would like to thank Jan Muehlbauer and Daniel Leighton, who have gone above and beyond any and all expectations. Working beside them and learning from their experience and knowledge was of great value throughout my research, while discussions bore the fruits of personal knowledge and growth I will value and use throughout my life. As the spirit of collaboration was strong throughout my research lab experience, I would like to personally thank the many fruitful discussions with, and lending hands of Daniel Bacellar, Magnus Eisele, Sahil Popli, Suxin Qian and James Daniel Spencer.

I would like to thank my advisors Dr. Yunho Hwang and Dr. Reinhard Radermacher for the time, guidance and support throughout my research and for offering me the opportunity to join the CEEE team (Center for Environmental Energy Engineering). In addition, I would like to thank my sponsors at Mainstream Engineering Corporation for the research opportunity and in particular, Ted Amundsen, for the positive feedback throughout my research exploration.

Finally, I would like to thank my amazing wife, Jarah Moesch, for making this journey possible, cheering me on every step of the way, supporting me in every way imaginable and sharing life’s journey with me. I look forward to our many future adventures together.

Table of Contents

List of Tables

List of Figures

Nomenclature

A	Area [m^2]
CFM	Cubic Feet per Minute [ft^3/min]
C_p	Specific Heat [kJ/(kg*K)]
C_v	Flow Coefficient
EB	Energy Balance [%]
g	Gravitational Acceleration [m/s^2]
H	Height [m]
h	Specific Enthalpy [kJ/kg]
h_{mean}	Mean Flow Boiling Heat Transfer Coefficient [$W/(m^2*K)$]
HD	Head [m]
L	Length [m]
LPM	Liters per Minute [L/min]
m	Mass [kg]
$\dot{m}$	Mass Flow Rate [g/s]
N	Number
P	Pressure [kPa]
ΔP	Pressure Differential [kPa]
q"	Heat Flux [W/m^2]
$\dot{Q}$	Heat Load [W]
RH	Relative Humidity [%]
SG	Specific Gravity [$(kg/m^3)/(kg/m^3)_{reference}$]
T	Temperature [°C]
ΔT	Temperature Differential [°C]
u	Uncertainty
W	Width [m]
x	R134a Mass Concentration [-]
x_q	Quality [-]

Greek Letters

ε	Effectiveness [-]	γ	Specific Weight [N/m^3]
η	Fin Efficiency [-]	$\dot{V}$	Volumetric Flow Rate [m^3/s]
ρ	Density [kg/m^3]		

Subscripts

#	Placement based on Figure 2.3	i	Inner
a	Air	l	Left
abs	Absorber	max	Maximum
atm	Atmospheric	min	Minimum
avg	Average	p	Planform
c	Center	R	R134a
ch	Channel	r	Right
ch,s	Channel Spacing	s	Surface
cond	Condenser	slhx	Solution Heat Exchanger
des	Desorber	slt	Solution Mixture
eff	Effective	sys	Systematic
evap	Evaporator	w	water
grid	Thermocouple Grid	wl	wall

Abbreviations

ABC	Absorption Cycle
ABS	Absorption System

ASHRAE	American Society of Heating, Refrigeration and Air-Conditioning Engineers
CFC	Chlorofluorocarbon
COP	Coefficient of Performance
DAQ	Data Acquisition System
DMA/DMAC	Dimethylacetamide
DMF	Dimethylformamide
EIA	U.S. Energy Information Administration
ETFE	Ethyl Tetrahydrofurfuryl Ether
FS	Full Scale
GWP	Global Warming Potential
H_2O/LiBr	Water/Lithium Bromide
HCFC	Hydrochlorofluorocarbon
HFC	Hydrofluorocarbon
MEC	Mainstream Engineering Corporation
NH_3/H_2O	Ammonia/Water
NIST	National Institute of Standards and Technology
OCR	Oil Concentration Ratio

ODP	Ozone Depletion Potential
PAG	Polyalkylene Glycol
PID	Proportional-Integral-Derivative
POE	Polyol Ester
VCC	Vapor Compression Cycle
VCS	Vapor Compression System

Chapter 1: Introduction

1.1. Energy Consumption

The current day search for alternative energy sources is a direct result of our ever increasing energy usage in conjunction with the depletion of our conventional energy sources. This energy crisis our world is facing is not a new topic. Since the industrial revolution we have seen a rise in fossil fuel production in direct correlation with global energy consumption [1]. In the past 30 years alone global fossil fuel primary energy consumption increased by 80% [2], while the EIA predicts that by the year 2040 global energy consumption will increase by an additional 56% [3].

Taking a step beyond the issue of depleting sources, fossil fuel production increases greenhouse gas concentrations that contribute directly to global warming. Fossil fuel burning has contributed to the increase of CO_2 (carbon dioxide) atmospheric concentration from 280 ppm, pre 1750, to a current 392.6 ppm (parts per million) through CO_2 emissions, currently at 9,167 MMT per year [4]. While methane levels, emitted during production and transport of fossil fuels, rose from 700 ppb, pre 1750, to a current 1,874 ppb (parts per billion) [4]. Although the concentration of methane is smaller, methane has a 21 times higher Global Warming Potential (GWP) than CO_2. These combined effects have been a significant force behind many energy saving and alternative energy source investigations.

Energy consumption broken down by sector reveals that in the United States buildings, residential and commercial, represent nearly 40% of the total energy consumption [5]. Energy consumption by usage reflects that 12-13% of the United

States building energy consumption is for cooling purposes [6]. In less moderate climates where ambient temperatures run higher than the average temperatures in the United States, such as: Delhi, India and Riyadh, Saudi Arabia, one would expect the cooling load percentage to increase. Comfort cooling has also been on a global rise as more homes install air-conditioning units due to personal economic growth [7]. In addition, with the economic growth of developing countries, more commercial buildings need cooling capabilities [8]. Based on demand and global growth trends, this market sector reflects a great potential in energy savings through increasing current cooling technology efficiencies and by directly reducing the fossil fuel energy consumption through the use of alternative energy resources.

1.2. Hybrid Absorption/Vapor Compression System

Conventionally, technologies utilize the vapor compression cycle (VCC) to provide the desired cooling capacity (Figure 1.1). The VCC takes the condenser sub-cooled working fluid, point 1, and expands it to a two-phase point at a lower pressure, point 2. The working fluid then flows through the evaporator to provide the desired cooling capacity, by removing the conditioned space heat load and transferring it to the working fluid, and exits the evaporator as a super-heated vapor, point 3. This super-heated vapor is then compressed to a higher pressure, point 4, through the use of a compressor. The high pressure super-heated vapor then flows through the condenser, rejecting its heat load to ambient conditions and exists as a sub-cooled liquid, point 1, to continue circulating through the VCC.

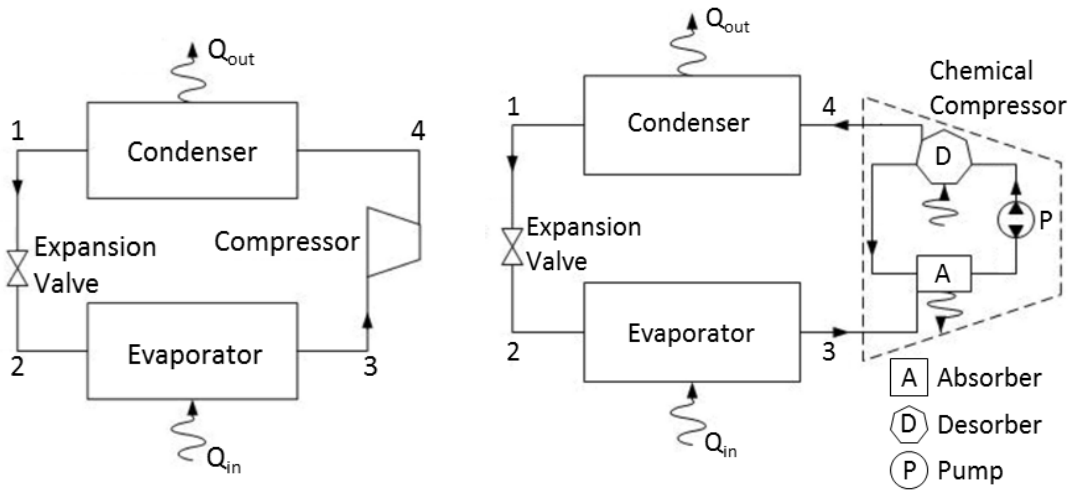

Figure 1.1: Vapor Compression Cycle (left) versus Absorption Cycle (right)

The absorption cycle (ABC) is similar to the VCC in the effect that both compress a working fluid from a low to a high pressure in order to cycle the working fluid through and provide the desired cooling capacity. The two main differences between the cycles lay between points 3 and 4. The first difference is that an absorption cycle uses a heat driven chemical compressor, encompassing an absorber, pump and desorber, to deliver the higher pressure working fluid while the VCC utilizes a vapor compressor (Figure 1.1). The second difference is that an absorption cycle uses a working fluid pair, a solution mixture containing absorbent and absorbed components, while the VCC utilizes a single working fluid.

The ABC's chemical compressor components are further detailed in Figure 1.2. A single-effect, i.e. one stage, absorption cycle has two main solution mixture lines, poor (1 through 3) and rich (4 through 5). The rich solution contains higher concentrations of the absorbent component than the poor solution. The pump provides the pressure lift for the poor solution from low to high pressures, point 1 to 2. The high pressure low temperature poor solution is then pre-heated by a solution

heat exchanger upon its entrance to the desorber, point 2 to 3, exchanging the heat and pre-cooling the high pressure high temperature rich solution upon its exit from the desorber, point 4 to 5. The high pressure midpoint temperature poor solution then enters the desorber, point 3, where heat and mass transfer occur due to a heat source, and exits as two separate streams, a high pressure high temperature rich solution, point 4, and high pressure high temperature refrigerant vapor stream, point 7. Point 7 to 10 is the same cycle described above using Figure 1.1, point 4 to 3. As mentioned, the high pressure rich solution then passes through the solution heat exchanger, point 4 to 5, and is expanded and dropped to a low pressure, point 5 to 6. The low pressure midpoint temperature rich solution then enters the absorber, point 6, where heat and mass transfer occur as it mixes with and re-absorbs the entering low pressure refrigerant vapor stream, point 10, while releasing heat to a heat sink. It then exits as a low pressure low temperature poor solution once again on its way to the pump to continue circulating through the cycle.

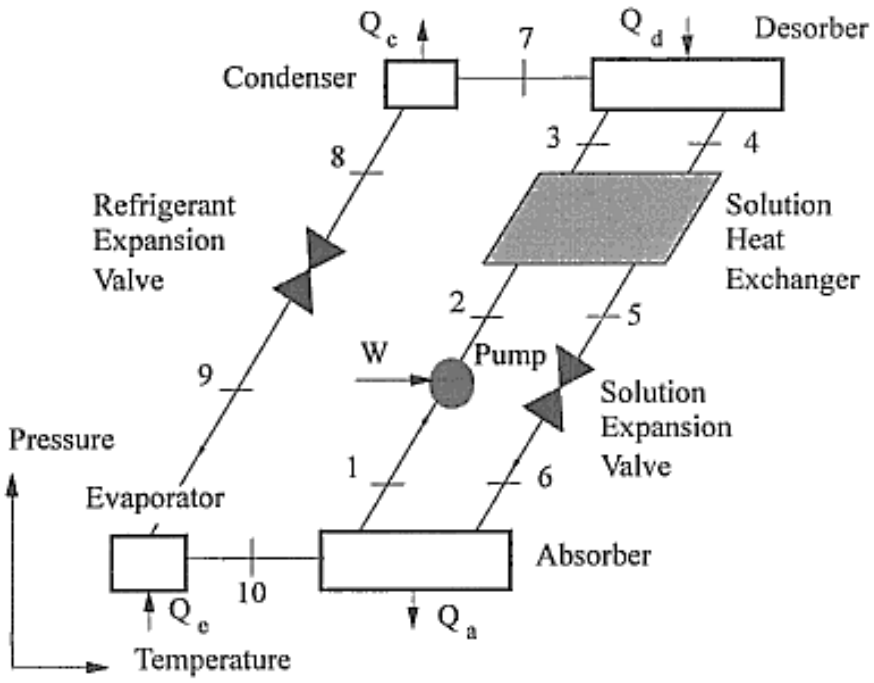

Figure 1.2: Single-Effect Absorption Cycle Schematic [9]

The use of a chemical versus vapor compressor makes the absorption system (ABS) larger than the vapor compression system (VCS), which along a higher coefficient of performance (COP) propelled the popularity of the VCS beyond that of the ABS in the mid 1900's. At the same time, the heat driven chemical compressor provides the advantage that has created a renewed interest in the ABS over the past two decades. As mentioned above, the chemical compressor of an ABS is heat driven versus mechanically driven, which makes the ABS advantage two-fold. On the one hand the heat can come from any source, limited by the fluid pair selection and matching desorption temperature. Therefore, waste heat can be utilized as the source. At the same time, the chemical compressor offsets the electric compressor power consumption, therefore directly reducing energy consumption and its associated toxins, as it is primarily fossil fuel sourced. The later making the ABS beneficial as

the energy consumption of the ABS is negligible compared to the VCS; electrically driven liquid pump versus vapor compressor.

Waste heat utilization is the primary advantage of the ABS as it uses unexploited heat streams, which otherwise get discarded to the environment. Due to the nature and efficiency of all thermodynamic processes, to produce work a process will have rejected heat. This rejected heat has a lower heating value, as in higher entropy, than a primary heat source, but its increased value lies in the fact that it is free and many times can still be utilized in another process, such as an ABS. Waste heat comes from many sources in various quantities and temperatures based on the originating process, making each waste heat stream viable for different applications. Considering power plant waste heat as an example, according to the EIA over the years of 2007-2011 coal, petroleum, natural gas and nuclear power plants had an efficiency range of 25-45%, depending on the prime mover [10]. Considering not all the losses result in waste heat, even a conservative 50% of the waste reflects a tremendous waste heat recovery source.

Hybrid absorption/vapor compression systems come in different configurations in order to combine the two cycles and their associated advantages. The main difference between the single effect hybrid systems is the mechanical compressor placement. Some hybrid configurations place the compressor between the absorber and desorber in order to provide additional refrigerant flow rate for enhanced performance while the absorption capacity cannot absorb it all [11]. Various hybrid configurations place the compressor between the desorber and condenser to promote higher vapor generation rates at lower desorption pressures,

while providing a high pressure lift to the condenser [12]. Other hybrid configurations place the compressor between the evaporator and absorber to provide the evaporator lower pressures, while giving a low pressure lift to the absorber to promote higher mass transfer, i.e. more vapor absorption, at higher absorption pressures [12, 13]. A simple parallel configuration offers the simplicity of small modifications to pre-existing VCS (Figure 1.3). As a combined cycle, the cooling capacity is shared by both cycles at different percentage splits depending on the changing cooling load. This simultaneously reduces the scale of the ABS and the VCS compressor load due to cooling capacity sharing, while still utilizing waste heat and maintaining higher system COP's than a stand-alone ABS.

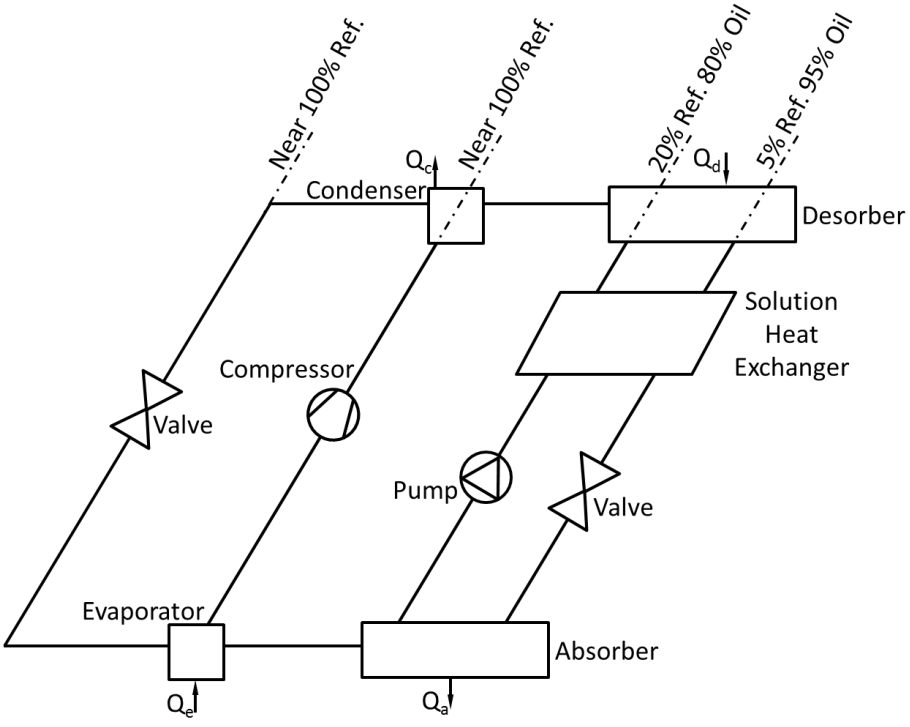

Figure 1.3: Hybrid Absorption/Vapor Compression System

Remote and off-grid applications present even more energy saving potential than the grid operated hybrid absorption/vapor compression system. Remote

applications tend to be off-grid, as they are not connected to the conventional electric grid and therefore use petroleum diesel powered generators to produce their needed electrical power. Offsetting diesel powered generator use entails reducing direct and indirect fossil fuel usage and its associated toxins. The direct reduction comes from reducing generator usage and indirect reduction from offsetting the transport of the fuel to the remote location. The usage of a generator to power a compressor presents in itself an opportunity. Diesel powered generator efficiencies range on average from 25-40%, where the remainder is wasted through exhaust gas, coolant, lubricant oil, frictional, convection and radiation losses [14, 15]. The major single source waste is in the form of exhaust gas, around 37%, with typical operating exhaust temperatures of 600-700°C [16, 17]. This generator exhaust can be directly utilized as the waste heat source for the absorption part of the system.

In conjunction with generator sourced power, remote and off-grid locations tend to be water source lean. Conventionally, absorbers are water cooled due to the water's large specific heat capacity, specifically four times higher than that of air. Taking into account the probable locative water limitation in addition to water management conservation, an air-cooled absorber can be utilized.

1.3. Mini-Channel Desorber

The ABS, as previously mentioned, is a larger system than the conventional VCS, which makes it a less attractive option. In an effort to make the ABS a more attractive option, promote its usage and therefore make waste heat recovery more prominent, the ABS must become more efficient and more compact. Therefore, component level study must be conducted to optimize their performance while

reducing their size, focusing on the two largest and major components; desorber and absorber.

Previous ABS studies include, but not limited to, the investigation of falling film heat exchangers [18-20], plate heat exchangers [20-23], tubular desorber [24] and mini/micro-channel heat exchangers [25-31]. Castro et al. (2009) compared falling film to bubble heat exchangers and found the latter performed better in both low and high solution mass flow rates [19]. Táboas et al. (2010) investigated a plate heat exchanger as a desorber and found the boiling heat transfer coefficient to be dominantly influenced by mass flux, versus heat flux and vapor quality, while the frictional pressure drop was equally influenced by mass flux and vapor quality; and heat flux played a small role [21]. García-Hernando et al. (2011) investigated pressure drop in a plate heat exchanger as a desorber and found the significant pressure drop to be a limiting factor in the usage of a plate heat exchanger as a desorber [22]. Balamurugan et al. (2012) studied both a plate and a tubular desorber and found that the plate outperformed the tubular since the heat and mass transfer effectiveness in the tubular desorber significantly reduced as the solution flow rate increased, while the change was not as pronounced in the plate desorber [23, 24].

Mini/micro-channel investigation has increased over the years due to the higher heat and mass transfer potential at smaller component sizing, while the increased pressure drop has been a point of contention. For clarification purposes, in this study the distinction between a mini-channel and micro-channel heat exchanger is made above and below the 1mm (hydraulic) diameter point, respectively. Field et al. (2006) studied two-phase adiabatic pressure drop and the effect of oil presence in a

micro-channel heat exchanger, with a 148 μm hydraulic diameter, and found that oil presence at high quality with low to medium mass flux had an increasing effect on pressure drop, while at high mass flux oil presence did not have a major influence due to the decreasing viscosity dependence [25]. Harirchian et al. (2009) studied the effect of channel dimension on flow boiling regimes in a micro-channel heat exchanger for 160-750 μm hydraulic diameters, finding that the heat transfer coefficient as a function of mass flux is nearly constant, with a wide range of heat flux values, at hydraulic diameters of 400 μm and above once nucleate boiling is dominant (unless dry-out occurs), while in hydraulic diameters below 400 μm nucleate boiling is suppressed at fairly lower heat fluxes [26].

Bowers et al. (1994) studied the differences between mini-channel and micro-channel heat exchangers at high heat fluxes and found that at similar critical heat flux values the mini-channel outperformed the micro-channel based on pressure drop values staying below the 1 kPa [27]. Nino et al. (2002) studied two-phase void fraction and frictional pressure drop in mini-channel heat exchangers with 1.02mm to 1.54mm hydraulic diameters, finding that even under constant mass flux and quality several flow regimes can be observed, which made previous separated flow model correlations not predict void fraction and pressure drop well, and therefore developed a most likely flow regime prediction model for void fraction and pressure drop [28]. Cavallini et al. (2005) studied two-phase frictional pressure drop for multiple refrigerants in a 1.4mm hydraulic diameter, while comparing experimental results to various models in literature and concluded that R134a has low pressure drops, less than 1 kPa, for mass flux as high as 1400 $kg/s*m^2$, which is fairly well predicted by

multiple correlations [29]. Determan et al. (2011) studied a mini-channel heat exchanger with inner diameter tubes of 1.067 mm and found it to be compatible for both the absorber and desorber with an overall heat transfer coefficient between 388-617 W/m^2*K while maintaining a low pressure drop [30]. In summary, a mini-channel heat exchanger with a 1 to 1.5mm hydraulic diameter appears to be a good choice for the desorber in order to minimize pressure drop, while maximizing heat and mass transfer along appropriate heat flux value selection in order to avoid critical heat flux. Although, as Zhang et al. (2010) pointed out, one must keep in mind that multiple correlation predictions and data sets are out there and in conflict with each other, therefore Zhang suggested their own two-phase frictional pressure drop and void fraction correlations [31].

1.4. Working Fluid Pair

ABS performance is fundamentally dependent on the working fluid selection. The chosen pair must have some basic properties, such as; miscible and stable within the operating conditions, a refrigerant with high heat of vaporization, a solvent with a high boiling point and mixture with reasonable viscosity and thermal conductivity, along with helpful qualities such as: non-corrosive, low cost and environmentally friendly. Throughout the history of the ABS the most commonly utilized pairs were NH_3/H_2O (ammonia/water) and H_2O/LiBr (water/lithium bromide). Various issues were encountered with these traditional fluids pairs, such as: additional required components, crystallization, freezing, vacuum conditions, corrosiveness and operating temperature limitations.

In the attempt to both improve the ABS performance and minimize its overall system size, many new working fluid pairs have been the topic of investigation. Over the past two decades a surge of investigations quickly moved towards the use of Hydrochlorofluorocarbons (HCFCs), such as R22, R123a and R124, as the refrigerant components since they were widely used in VCSs, finding them reasonably soluble in combination with various organic solvents, such as Dimethylformamide (DMF), Dimethylacetamide (DMA/DMAC) and Ethyl Tetrahydrofurfuryl Ether (ETFE) [32-35]. Murphy et al. (1984) found that R123a/ETFE showed good potential with a possible COP of 1.5 [32]. Fatouh et al. (1993) tested R22 in combination with multiple organic solvents and found that R22/DMF and R22/DMA had favorable performance taking into account cut-off temperatures, circulation ratio and COP [33]. Borde et al. (1997) tested R124 in combination with multiple organic absorbents and found R124/DMAC had superior performance based on COP and circulation ratio in a single-stage absorption cycle [35].

Over the past decade alternative solution exploration shifted quickly towards Hydrofluorocarbons (HFCs) as the refrigerant component due to the enforcement of the Montreal Protocol, which is phasing out the use of HCFCs along with CFCs due to their ozone depletion potential (ODP). R134a became a focus of many investigations. As all HFCs, R134a has an ODP of zero. Borde et al. (1995) tested R134a in combination with multiple organic absorbents and found the COP's to be of very similar values, while the R134a/DMTEG stood out as the combination with the lowest circulation ratio [36]. Wahlstrom et al. (1999) studied the solubility of various HFCs in a pentaerythritol tetrapentanoate ester (PEC9) over a 50 to 1900 kPa

pressure range and a 30 to 90°C temperature range and found that R152a had the highest solubility followed by R134a [37]. Wahlstrom et al. (2000) repeated the same solubility study of various HFCs in three different Polyol Ester (POE) oils over a 70-2,100 kPa pressure range and a 30-90°C temperature range and found the same solubility performance order [38]. Marsh et al. (2002) reviewed the advantages and disadvantages associated with using HFCs (versus HCFCs) in conjunction with mineral versus synthetic oils, addressing the fact that HFC refrigerants have low solubility with mineral oils while having higher solubility with synthetic lubricants along with less phase separation [39]. In addition, the lubricant comparison revealed advantages of using the POE lubricants; their environmental benefits, as they can be synthesized from renewable resources and is biodegradable, and their reduced hygroscopic and higher miscible properties versus Polyalkylene Glycol (PAG) lubricants. Yokozeki (2005) studied R134a in combination with various absorbents, finding that based on COP and circulation ratio R134a/DMF is a promising absorption fluid pair, while due to DMF's relatively low normal boiling point a rectifier might be required just as the NH_3/H_2O mixture [40]. Mainstream Engineering Corporation (MEC) studied R134a in combination with both POE32 and 1-Ethyl-3-Methylimidazolium Tetrafluoroborate ($EMIMBF_4$), finding that the POE32 exhibited more favorable absorption parameters and that R134a/POE32 is a more favorable combination due to lower cost and its wide usage in current VCSs, which simplifies material compatibility [41]. The selection of R134a/POE32 as the working fluid pair also offers the avoidance of crystallization issues while using an air-cooled absorber.

1.5. Objectives

In conclusion of the above literature review the following two objectives have been established for this investigation:

- Design and construct a test facility to experimentally investigate the performance of a mini-channel desorber with an R134a/POE32 solution mixture, under off-grid high temperature conditions, while simulating the operational conditions of a hybrid absorption/vapor compression system with an air-cooled absorber.
- Conduct an experimental parametric study investigating the effect of temperature, pressure, solution mass flow rate and refrigerant concentration variations on desorber and desorption performance through the analysis of vapor generation, circulation ratio, poor solution concentration, desorber mean heat transfer coefficient and desorber quality difference.

Chapter 2: Test Facility

An experimental test facility is designed and constructed in order to investigate the potential of a specific theoretical endeavor. As such, the design and construction phase must bridge between the theory and practice by taking into account material compatibility limitations and operating conditions at which the facility will be tested. This chapter describes the process through which these operating conditions were established, followed by the related system component load calculations and selection process.

2.1. Test Conditions

The test facility was designed to test the performance of a mini-channel desorber while simulating a hybrid absorption/vapor compression system. Keeping this in mind, the condenser and evaporator temperatures and corresponding saturation pressures, determined by the outside conditions and desired indoor condition, respectively, were the deciding and starting factors for system design. On the condenser side, a pressure range was established after considering that ambient temperature of 35°C will be acting as the condenser's heat sink (Figure 2.1), along with a minimal 5°C subcooling (Table 1) [41]. For the evaporator, a maximum indoor temperature of 25°C was chosen as the evaporator's heat source (Figure 2.1) based on ASHRAE comfort zone [42]. Combined with the maximum desired evaporator cooling capacity of 3.5 kW and a minimal 5°C superheat, an evaporator pressure range was established (Table 1) [41].

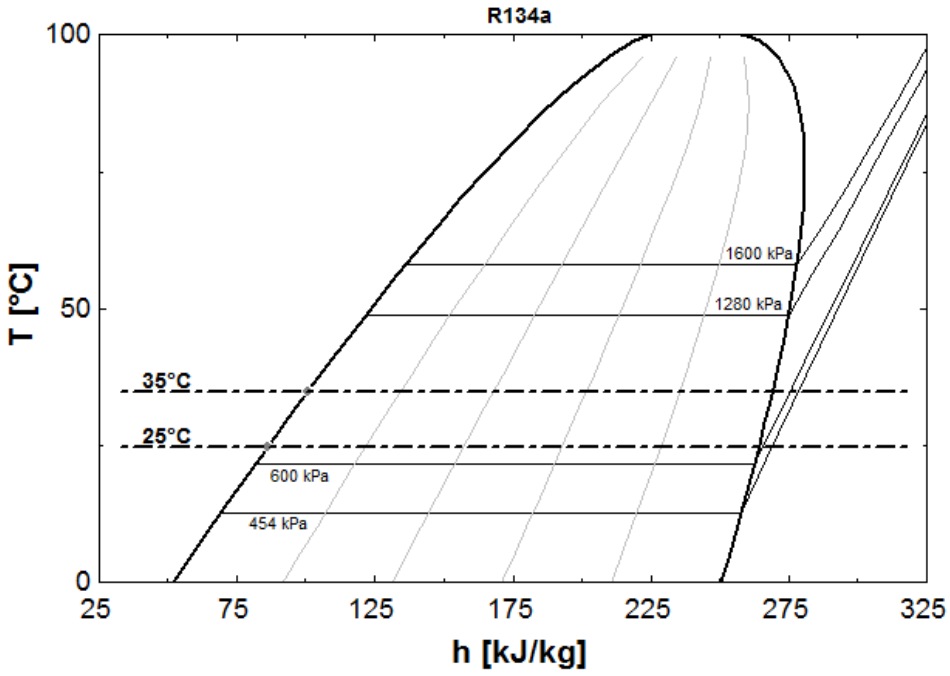

Figure 2.1: R134a Temperature-Enthalpy Property Diagram

Once the condenser and evaporator pressure ranges were established, the absorption cycle was simulated in CHEMCAD. The CHEMCAD software has the input capability of solution mixture equilibrium data and thermo physical property calculations with built in Equation of State (EOS), therefore it was chosen as the appropriate simulation software for the facility design and component sizing phase. R134a/POE32 equilibrium data was imported into CHEMCAD [41]. A cycle with the appropriate components was compiled and run (Figure 2.2) to establish each component's maximum load and the facilities design parameters of mass flow rates, pressures, temperatures and expected vapor generation (Table 1).

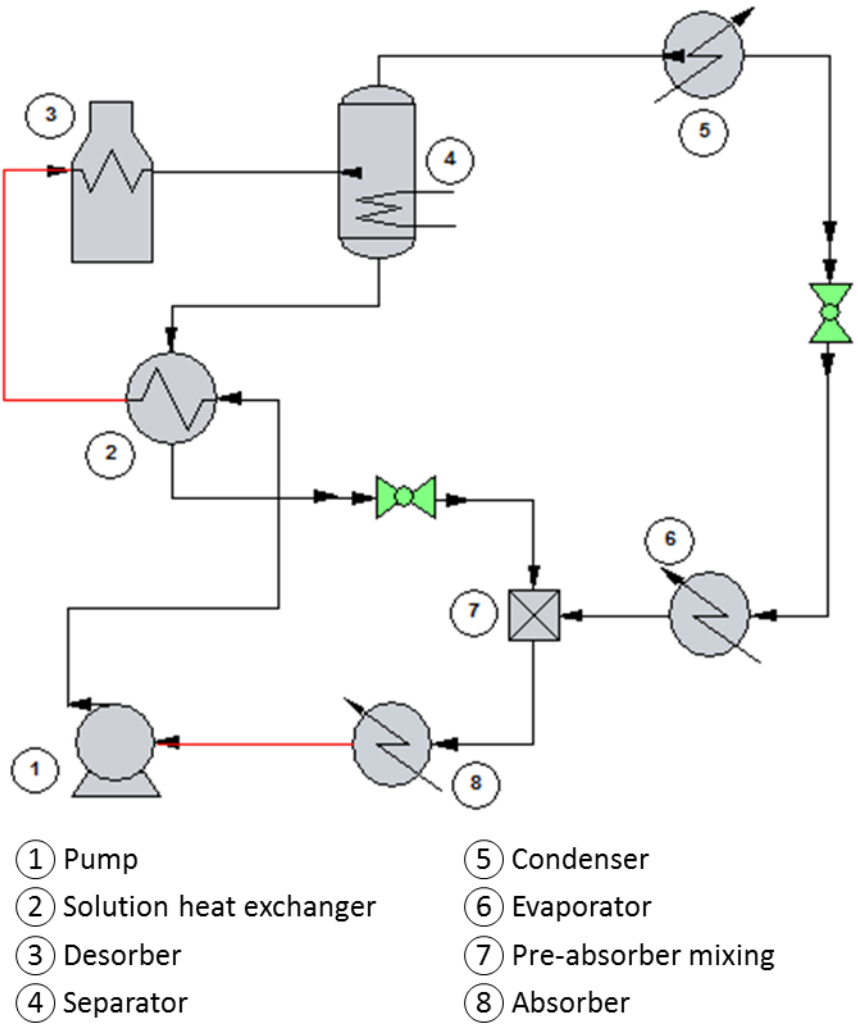

Figure 2.2: CHEMCAD Schematic

Table 1: Design Parameters

Parameter	Range	Location
Pressure, high side [kPa]	1,280-1,600	Desorber and Condenser
Pressure, low side [kPa]	454-600	Absorber and Evaporator
Temperature, high side [°C]	120-150	Desorber outlet and Condenser inlet
Temperature, low side [°C]	43-49	Absorber outlet
Temperature, air-side [°C]	35	Wind tunnel (Absorber inlet)
Mass Flow Rate [g/s]	52-140	Pump (poor solution)
Vapor Flow Rate [g/s]	1-21	Refrigerant loop (Expected)

The facility's construction incorporates four sections: a solution loop compiled of poor and rich solution sub-sections, a wind tunnel constructed with the purpose of cooling the absorber at the design ambient temperature of 35°C, a refrigerant loop for generated vapor separation running in parallel with the rich solution sub-section and a water loop serving as both a cooling and heating source for various components. Once the facility's design parameters were established in CHEMCAD, each loop component was appropriately selected considering the R134a/POE32 solution mixture material compatibility, its CHEMCAD theoretically calculated load and the temperature and pressure ranges it is expected to operate in.

2.2. Solution Loop

The solution loop is the chemical compressor of the absorption cycle as it replaces the compressor of the vapor compression cycle by absorbing the vapor into a rich solution mixture, pumping it through a liquid pump and then desorbing the vapor back out. The main components of the solution loop are a pump, solution heat exchanger, desorber, post-heater, separator, pre-cooler, absorber and receiver. A design schematic was created considering all involved components and necessary measurements for data collection (Figure 2.3). Throughout the writing, a rich solution refers to higher concentrations of the absorbent component, i.e. rich in POE32 oil, where a poor solution refers to lower POE32 concentrations since it contains higher R134a concentration.

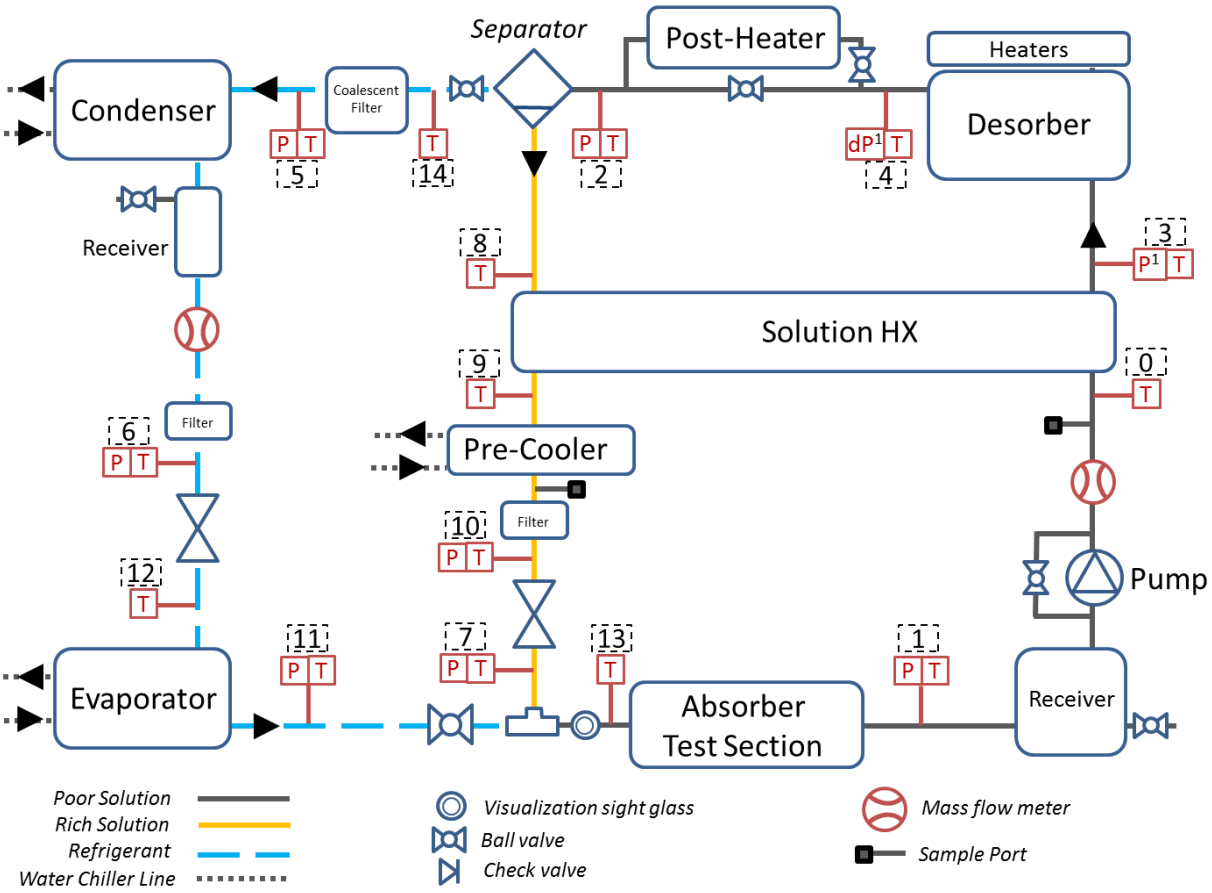

Figure 2.3: Solution and Refrigerant Loop Schematic

As the driving pressure differential force of the system, the pump selection must take into account head based on maximum desired system pressure difference and fluid properties (Equation 1), and desired system flow rates (Equation 3). Based on the results of Equation 1 through Equation 3, a Hydra-Cell M03X diaphragm type pump was selected with a 0.569-11.3 LPM flow rate range, maximum inlet/outlet pressures of 1,724/6,895 kPa and material construction, brass and neoprene, compatible with the R134a/POE32 solution (Figure 2.4). A diaphragm type pump was selected over a gear pump due to the highly viscous R134a/POE32 mixture property. The pump speed was controlled utilizing a variable frequency drive.

$$HD = \frac{\Delta P_{max}}{\gamma_{slt}} = 117\ m \qquad \text{Equation 1}$$

$$\gamma_{slt} = \rho_{slt} * g = 9{,}810 \frac{Pa}{m} \qquad \text{Equation 2}$$

$$\dot{V}_{slt} = \frac{\dot{m}_{slt}}{\rho_{slt}} = 3.4\ to\ 8.4\ LPM \qquad \text{Equation 3}$$

Figure 2.4: Hydra-Cell M03X Diaphragm Pump

The importance of the solution heat exchanger lies in its simultaneous pre-heating of the poor solution mixture on its way to the desorber while pre-cooling the rich solution mixture on its path to the absorber. This heat recovery process improves the overall ABS performance. When selecting the appropriate heat exchanger, the calculated theoretical load and solution mixture were taken into account, along with practical heat exchanger effectiveness values (Equation 4). Considering physical component sizing limitations and the maximum CHEMCAD theoretical load, a GEA FG10X20-24 brazed plate heat exchanger with a maximum capacity of 8 kW, at design conditions, was selected for the solution heat exchanger (Figure 2.5). This selection was coupled with a GEA FG5X12-14 brazed plate heat exchanger with a maximum capacity of 5.5 kW acting as a pre-cooler, utilizing cold water to cool the

rich solution exiting the solution heat exchanger on its way to the absorber, on an as-needed-basis (Figure 2.6).

$$\varepsilon_{SHX} = \frac{T_8 - T_9}{T_8 - T_0} \qquad \text{Equation 4}$$

Figure 2.5: GEA FG10X20-24 Solution Heat Exchanger

Figure 2.6: GEA FG5X12-14 Solution Heat Exchanger

As the point of heat input to the poor solution and vapor generation, the desorber is a key component in an absorption facility. The desorber used in this experimental facility was a mini-channel heat exchanger designed and fabricated by

MEC (Figure 2.7). The desorber dimensions are presented in Table 2. In this experimental facility thin film heaters were used to simulate the actual use of generator exhaust over the desorber. Based on a 3 kW maximum capacity heat input requirement, Birk Manufacturing thin film heaters were selected (Figure 2.8), with a1.5 kW capacity per heater placed on each side of the desorber. Each thin film heater was controlled utilizing a variable frequency transformer in order to adjust its heat output.

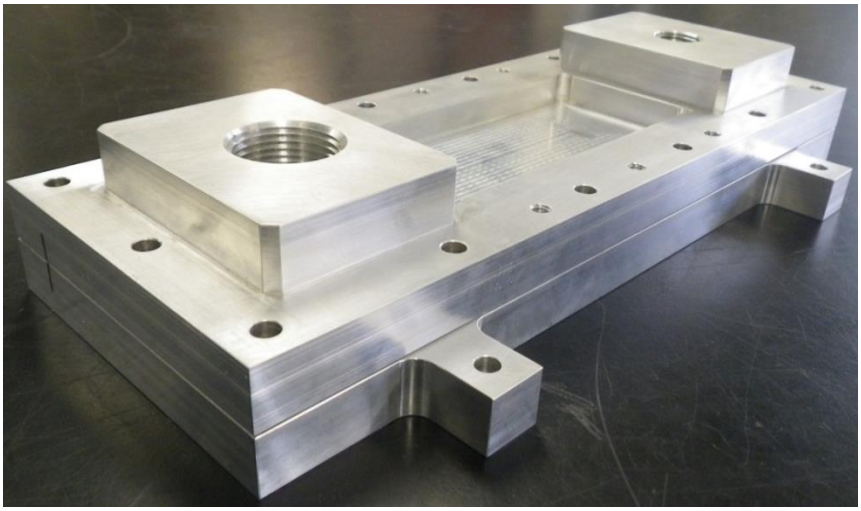

Figure 2.7: MEC Mini-Channel Desorber

Table 2: Desorber Geometry

Item	Value
Tube number	2
Channels per tube	52
Channel width	0.84 mm
Channel width spacing	0.038 mm
Channel height	1.40 mm
Channel length	150 mm

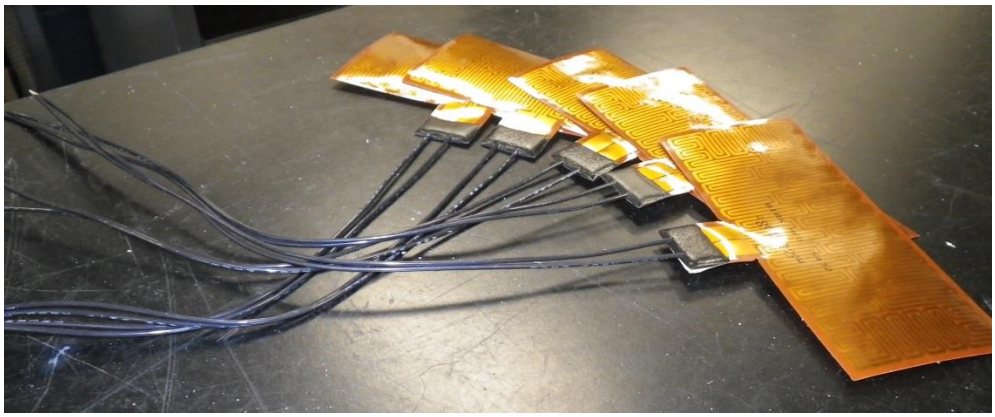

Figure 2.8: Birk Manufacturing Thin Film Heaters

For supplemental poor solution heating capacity, a Warren Electric XRS-4.4 immersion heater was selected with a 4.4 kW capacity (Figure 2.9). The additional capacity was originally designed to achieve the higher range of system temperatures at the desorber outlet/separator inlet, anticipating that the solution heat exchanger will not be sufficient for bringing the poor solution to high enough temperatures at the desorber inlet. After initial testing, the supplemental heater, acting originally as a pre-heater to the desorber, was re-positioned as a post-heater after the desorber. In this configuration, the post-heater allows the desorber to operate in the first half of the quality range versus the second half; addressing and preventing any possible mini-channel heat exchanger dry out in the desorber. It then acts as a secondary desorber, on an as-needed-basis, to bring the poor solution to the higher system temperatures at the separator inlet. One of the two heating elements in the post-heater was turned on or off using a manual switch, while the second element was controlled utilizing a variable frequency transformer in order to easily adjust its heat output.

Figure 2.9: Warren Electric XRS-4.4 Immersion Heater

The separator is a critical component in an absorption cycle as it receives the poor solution at its highest temperature as a vapor and saturated solution mixture and needs to separate the stream into refrigerant vapor and rich solution parallel output streams. For the separator vessel a Swagelok 304L-HDF8-2250 high pressure vessel was selected with four different inlets and outlets (Figure 2.10). The top vertical connection was used as the poor solution inlet, the top angled connection was used as the vapor outlet, the bottom connection as the rich solution outlet and the top horizontal connection was utilized for a parallel connection for separator liquid level sensing. The top vertical separator inlet was modified by inserting an angled copper tube through the inlet and spraying the incoming poor solution at the separator wall in order to allow all generated vapor to escape the incoming stream and appropriately exit towards the refrigerant loop.

Figure 2.10: Swagelok 304L-HDF8-2250 Pressure Vessel, as Separator

Once the high pressure rich solution stream was separated by the separator and cooled by the solution heat exchanger it needed to be dropped in pressure before it entered the absorber. Taking into account the solution mixture properties, expected system pressure drops and flows, a C_v range was calculated (Equation 5). For flow control and pressure drop a Swagelok SS-1RS6 regulating needle valve was selected with a linear C_v versus turns relationship encompassing the calculated values. The needle valve was coupled with a Handbay MCL-050AB-1 actuator with 180 steps per each full turn, insuring accurate and sensitive control over the wide condition range (Figure 2.11). A manual needle valve controlled by an actuator versus an electronic expansion valve was chosen due to the higher design temperatures.

$$C_v = \dot{V}\left(\frac{SG}{\Delta P}\right)^{\frac{1}{2}}$$ Equation 5

Figure 2.11: Swagelok SS-1RS6 Regulating Needle Valve Controlled by a Handbay MCL-050AB-1 Actuator

An absorber plays a crucial role in an absorption facility as the point at which vapor is absorbed by a rich solution liquid stream before it is delivered to the liquid pump for another cycle round. The approach for this experiment was to pre-mix the rich solution with the vapor stream just before entry to the absorber. A pre-mixing chamber design schematic was created considering all involved components (Figure 2.12). A 20 micron convex sintered metal filter was used as a gas sparger and placed in the path of the rich solution liquid stream as it enters the mixing chamber to facilitate the removal of newly formed gas bubbles from the sparger surface. The pipe diameter was reduced at the gas and liquid contact surface location, thereby increasing the fluid velocity, to promote faster gas bubble removal rates from the sparger. Three sight glasses were placed at the two inlets and exit of the mixing chamber for visualization (Figure 2.13).

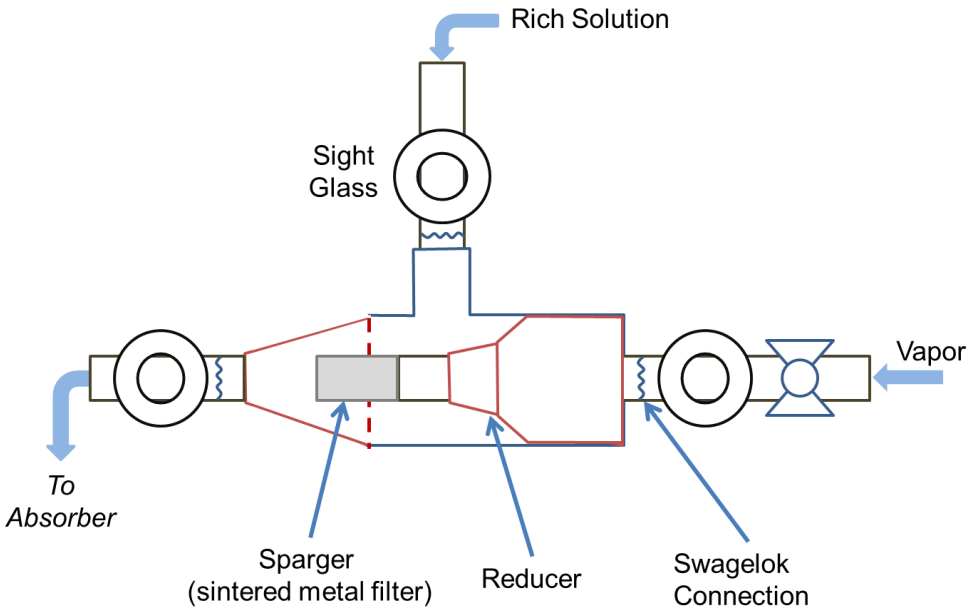

Figure 2.12: Pre-Absorber Mixing Chamber Schematic

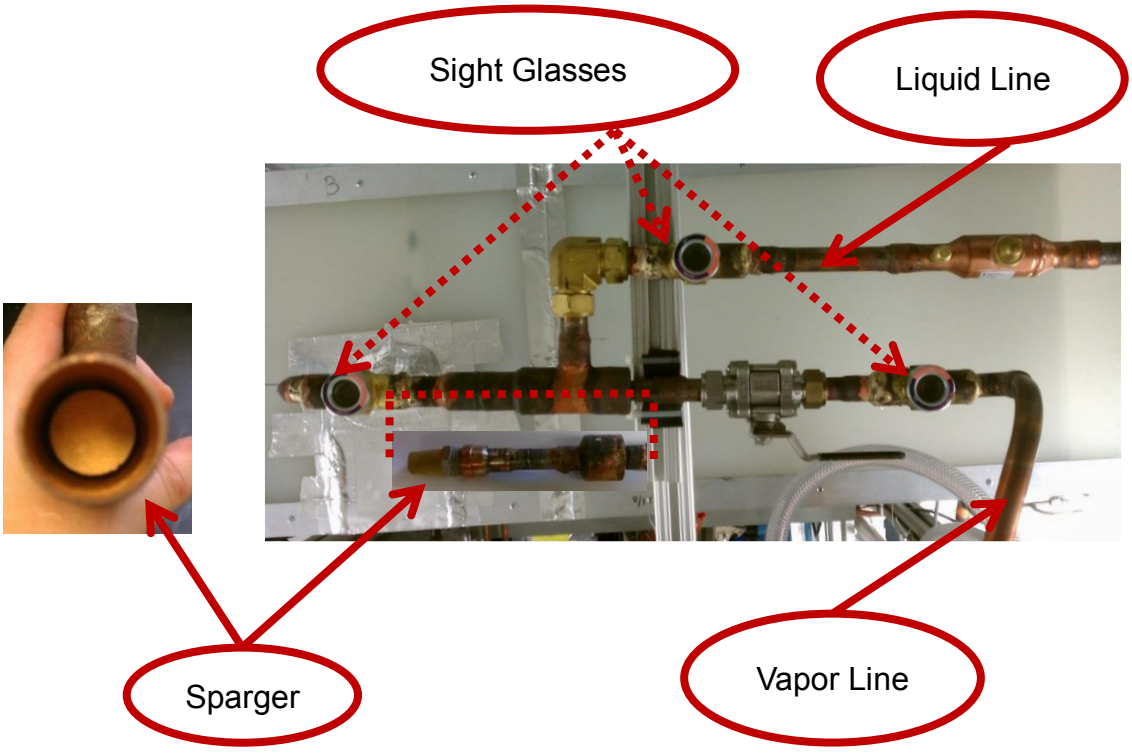

Figure 2.13: Pre-Absorber Mixing Chamber

For the absorber heat exchanger it was desired to utilize off the shelf micro-channel heat exchangers with a maximum load of 4.5 kW, while air cooling the absorber at a design temperature of 35°C. The absorber used in this experimental facility was supplied by MEC as two micro-channel heat exchangers in parallel (Figure 2.14).

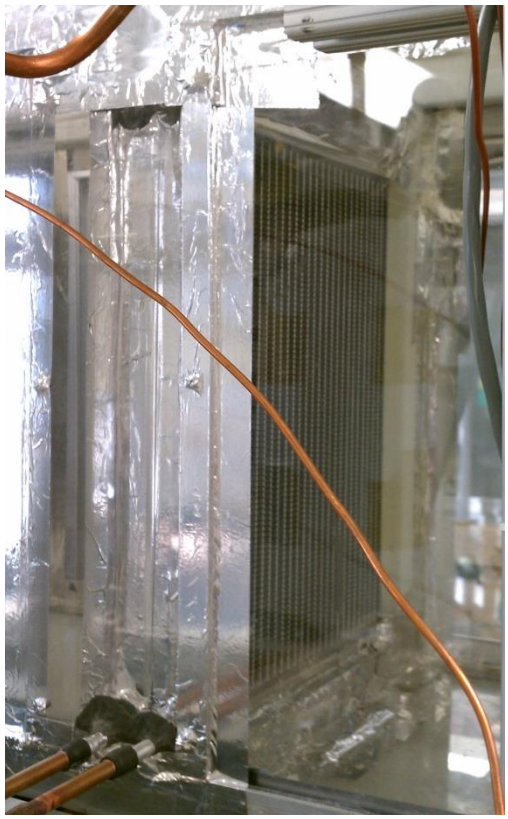

Figure 2.14: MEC Supplied Micro-Channel Absorber

The receiver is an essential component in an absorption cycle as it receives the poor solution from the absorber on its way to the pump and ensures that any vapor not fully absorbed in the absorber does not enter the pump. For this purpose a Swagelok 304L-HDF8-2250 pressure vessel was selected (Figure 2.15). The selected receiver did not have an integrated level sensor therefore a parallel connection was created out of sight glasses (Figure 2.15).

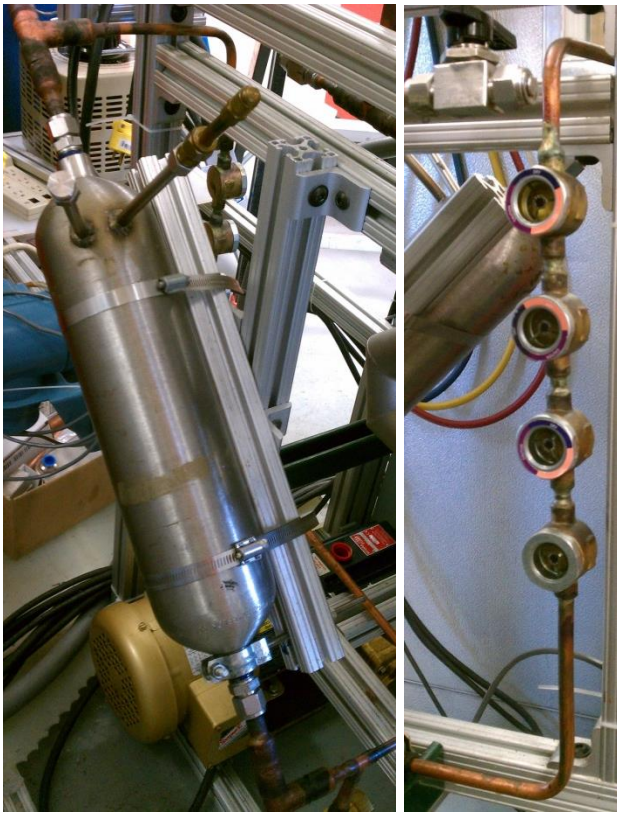

Figure 2.15: Swagelok 304L-HDF8-2250 Pressure Vessel as Receiver with Parallel Liquid Level Visualization

Equilibrium concentration data verification requires a sampling methodology. Based on ASHRAE standard 41.4 a sample port and vessel schematic was created for appropriate sample mass fraction measurement (Figure 2.16) [43]. System connection points were placed on both poor and rich solution sides (Figure 2.3). For appropriate sample size a Swagelok 304L-HDF4-300CC cylinder was chosen (Figure 2.17). Quick and proper connection to the system was achieved using compression fittings, quick sample timing was maintained using ball valves and a needle valve was utilized for appropriate refrigerant discharge.

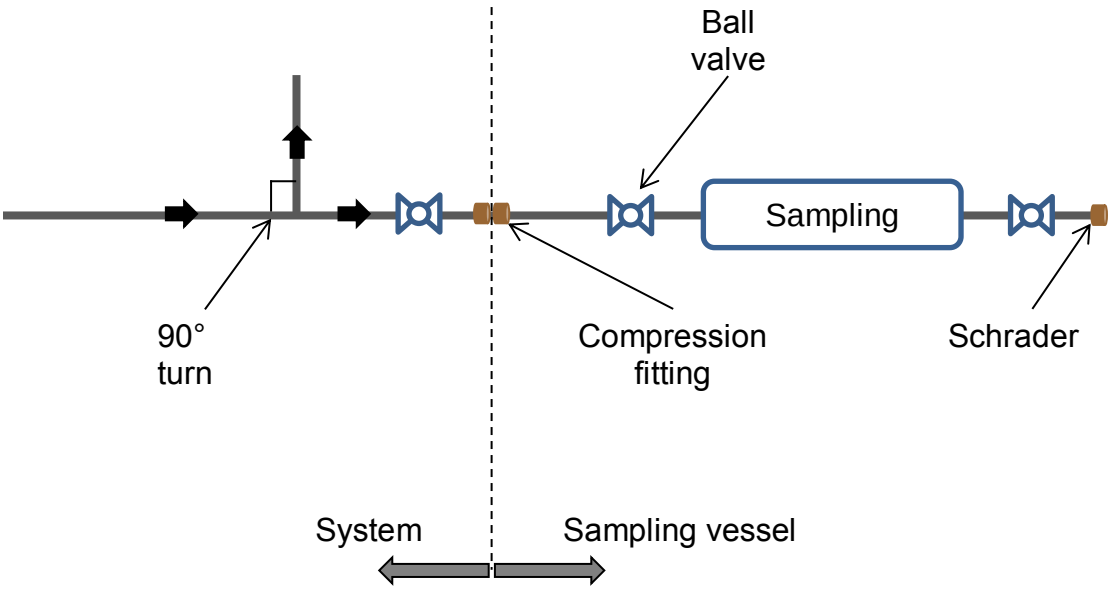

Figure 2.16: Sampling Port and Vessel Schematic

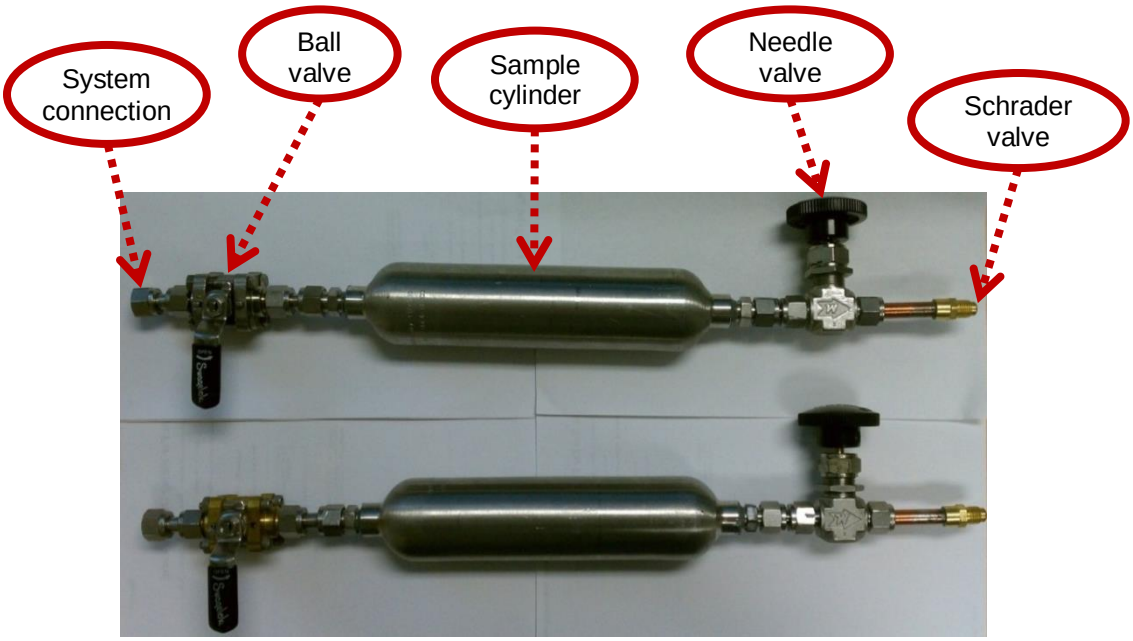

Figure 2.17: Sampling Vessel Construction

2.3. Wind Tunnel

In this experimental facility the absorber is to be air cooled by forced convection at a design temperature of 35°C. For appropriate air side measurements a

wind tunnel was designed based on ASHRAE standard 41.2 for calorimetric (heat exchanger) chambers [44]. The main components of the wind tunnel are air straighteners, a heater, mixers and a suction fan. A design schematic was created considering all involved components and necessary measurements for data collection (Figure 2.18).

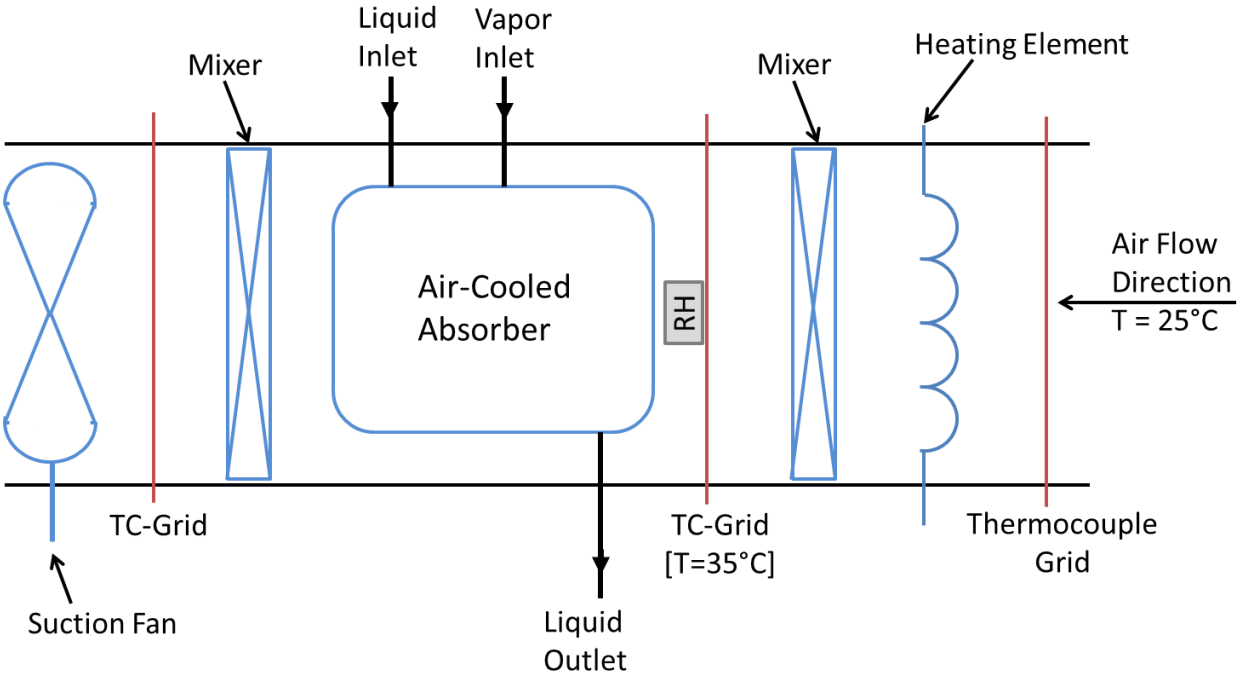

Figure 2.18: Wind Tunnel Schematic

The significance of an air straightener is in its function of providing uniform mass distribution throughout the wind tunnel. Combined with the need for appropriate temperature measurement throughout the wind tunnel, three thermocouple grids comprised of a straightener and nine evenly distributed thermocouples each, were created and placed at their designated locations (Figure 2.19).

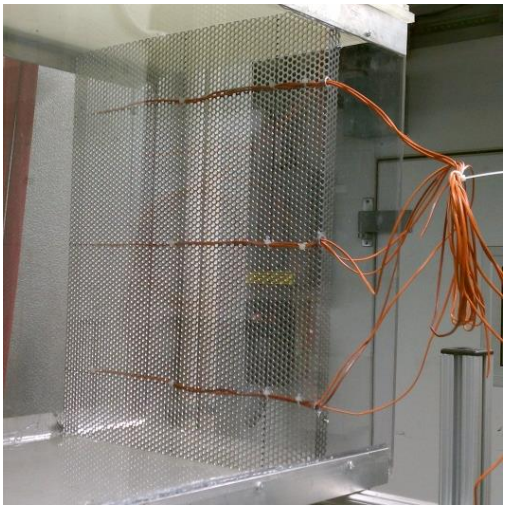

Figure 2.19: Thermocouple Grid

The heater's importance lies in it heating the wind tunnel's incoming room temperature air up to the design temperature of 35°C for the absorber inlet. Assuming the room temperature will be maintained at 25°C and taking into account the maximum absorber heat load and corresponding air flow rates, a maximum heat input of 3.5 kW was calculated (Equation 6). For this capacity a Farnam DH12-4-240-1air-heater was selected with a 4 kW capacity (Figure 2.20). Five of the six heating elements in the air-heater were turned on or off using individual manual switches, while one element was controlled utilizing a variable frequency transformer in order to easily adjust its heat output.

$$\dot{Q} = \rho \dot{V} C_p \Delta T_{air} \qquad \text{Equation 6}$$

Figure 2.20: Farnam DH12-4-240-1 Air-Heater

The significance of a mixer is in eliminating temperature stratification before every temperature measurement point. For this purpose and to minimize pressure drop throughout the wind tunnel, a Blender Products AB-10 static air mixer was selected with a nominal 0.283-0.354 m^3/s air flow rate range (Figure 2.21). A minimal 20 Pa pressure drop per mixer was calculated at the wind tunnel's 0.307 m^3/s maximum expected air flow rate (Equation 7).

$$\Delta P_{actual} = \Delta P_{chart} \left(\frac{CFM_{actual}}{CFM_{chart}} \right)^2 \qquad \text{Equation 7}$$

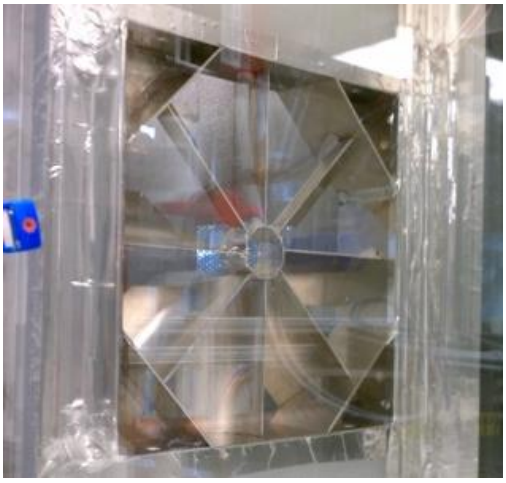

Figure 2.21: Blender Products AB-10 Static Air Mixer

As the driving air flow force of the wind tunnel, the fan selection must provide appropriate air flow rates for absorber cooling while overcoming the pressure drops throughout the wind tunnel (Equation 8). Using the maximum CHEMCAD calculated absorber load of 4.5 kW and taking into account that the resulting absorber air outlet temperature combined with the solution side temperatures cannot violate the first law of thermodynamics, a 0.307 m^3/s maximum expected air flow rate was calculated (Equation 6). Based on a total 320 Pa pressure drop in the wind tunnel along with a 0.307 m^3/s maximum expected air flow rate, a Dayton 7AV25 suction fan was selected with a maximum 0.448 m^3/s rated air flow at 320 Pa pressure drop (Figure 2.22). The fan speed was controlled utilizing a variable frequency drive.

$$\Delta P_{wind\ tunnel} = 3 * \Delta P_{straightner} + 2 * \Delta P_{blenders} + \Delta P_{absorber} \qquad \text{Equation 8}$$

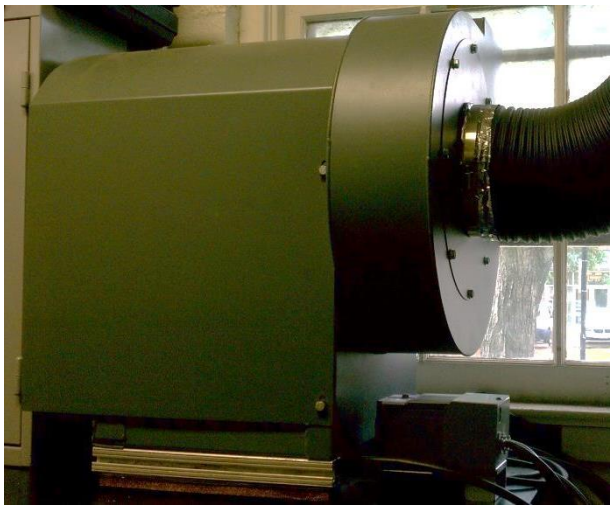

Figure 2.22: Dayton 7AV25 Suction Fan

2.4. <u>Refrigerant Loop</u>

The refrigerant loop is the absorption cycle loop that mirrors the vapor compression cycle, excluding the compressor, to provide its resulting cooling capacity. The main components of the refrigerant loop are the condenser, expansion

valve and evaporator. A design schematic was created considering all involved components and necessary measurements for data collection (Figure 2.3). On account of possible R134a/POE32 separation difficulties, stemming from increased solubility, and the associated evaporator performance decrease due to oil presence [45], an additional filter was installed at the separator vapor outlet to assist in oil droplet filtration and prevent excess POE32 from entering the refrigerant loop. For this purpose a Temprite 131 coalescent filter was chosen (Figure 2.23).

Figure 2.23: Temprite 131 Coalescent Filter

The condenser receives the high pressure generated R134a vapor from the separator and cools it down to sub-cooled liquid before it enters the expansion valve. Taking into account the maximum condenser load of 5.8 kW, the R134a working fluid and water as the cooling fluid, a GEA C1/2AG-8 brazed plate heat exchanger was chosen with an over 6 kW capacity at design conditions (Figure 2.24). A Swagelok 304L-HDF4-1000 pressure vessel, acting as a receiver, was selected and placed between the condenser and the expansion valve in order to ensure that only

liquid enters the expansion valve and to provide volumetric variation capacity for changing R134a charges (Figure 2.25).

Figure 2.24: GEA C1/2AG-8 Condenser

Figure 2.25: Swagelok 304L-HDF4-1000 Pressure Vessel as Receiver

Once the high pressure R134a stream has been sub-cooled by the condenser it needs to be dropped in pressure before it enters the evaporator. For flow control and pressure drop a Sporlan SER1.5 electric expansion valve was selected with 3,500 steps ensuring that fine control can be accomplished over the wide design condition range (Figure 2.26).

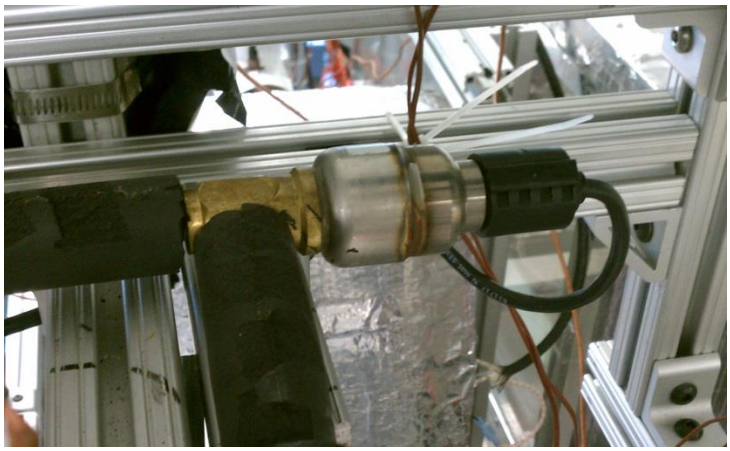

Figure 2.26: Sporlan SER1.5 Electric Expansion Valve

The evaporator is where the cooling capacity is provided by removing the heat load from the desired location and transferring it to the working fluid. The evaporator receives the low pressure saturated R134a liquid from the expansion valve and heats it up to super-heated vapor, utilizing hot water as the heating load in this experiment, before it re-enters the absorber and gets absorbed by the rich solution. Taking into account the desired maximum evaporator load of 3.5 kW, the R134a working fluid and water as the heating fluid, a GEA FG5X12-4 brazed plate heat exchanger was chosen with a maximum capacity of over 4 kW at design conditions (Figure 2.27).

Figure 2.27: GEA FG5X12-4 Evaporator

2.5. Water Loop

In this experiment, the water loop was designed to serve as the cooling source for both the condenser and pre-cooler while simultaneously serving as a heating source for the evaporator. The main components of the water loop are the chiller, pump and water heater. A design schematic was created considering all involved components and necessary measurements for data collection (Figure 2.28).

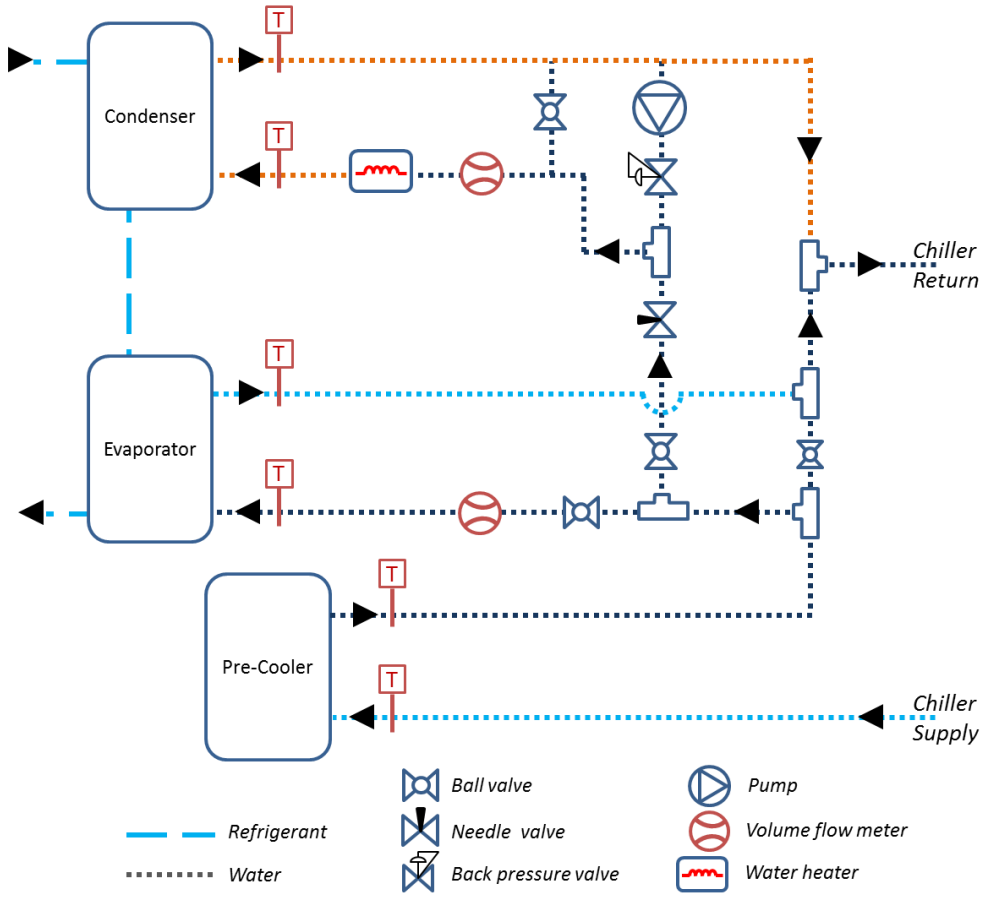

Figure 2.28: Water Loop Schematic

The water loop begins by entering the pre-cooler directly from the water chiller, it then exits from the pre-cooler at a higher temperature and splits; some going to the evaporator, some to the condenser while some returning to the chiller. The condenser and evaporator flow rates are controlled by ball and needle valves, while

the total flow through the pre-cooler is controlled directly by the chiller. The condenser also has an internal loop with a pump, while still having a parallel connection to the chiller line, allowing the condenser to heat up its own water to higher temperatures as needed. The pre-heated water from the pre-cooler outlet in conjunction with the internal loop reduces the condenser water heater load significantly. For this purpose a water heater was constructed from a 2.7 kW heating element and 80 schedule PVC (Figure 2.29). The chiller capacity must be able to cool down all combined returning water to the desired pre-cooler inlet temperature. For this purpose a Neslab HX-500 chiller with a total cooling capacity of 15.7 kW was selected (Figure 2.30).

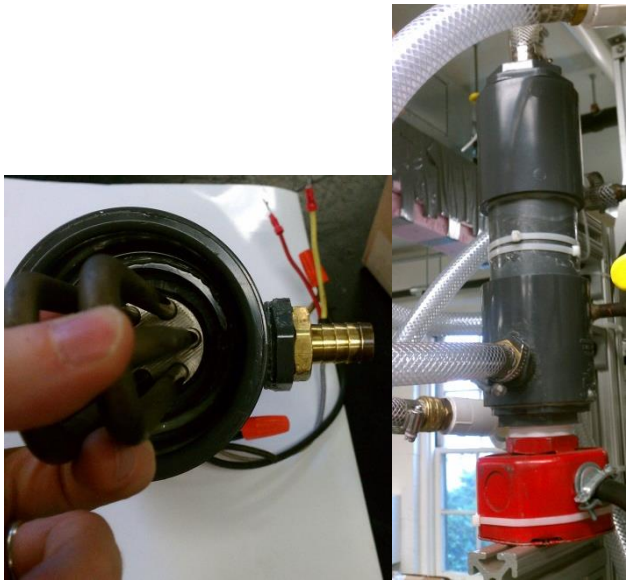

Figure 2.29: Constructed Water Heater

Figure 2.30: Neslab HX-500 Chiller

2.6. Instrumentation

To evaluate the desorber and system performance various measurements were taken (Figure 2.3, Figure 2.18 and Figure 2.28). These measurements were then utilized to obtain refrigerant properties and calculate refrigerant concentration, density and energy balances. The importance of appropriate measurements and their corresponding accuracy lies in the necessity of valid data for appropriate performance evaluation.

2.6.1. Pressure Transducers

Three different pressure transducer models were utilized throughout the facility (Figure 2.31). In addition, a barometric pressure transducer was utilized since seven of the 10 pressure transducers were gauge transducers (Figure 2.32). Each model's range, accuracy and system location is presented in Table 3.

Figure 2.31: Setra C206, Setra 280E and Wika S-10 Pressure Transducers (left to right)

Figure 2.32: Cole-Parmer 98072-38 Barometric Pressure Transducer

Table 3: Pressure Transducer Specifications

Model	**Range**	**Accuracy (FS)**	**Location** (Figure 2.3**)**
Setra C206	0 - 3447 kPa gauge	±0.13%	3, 6, 7, 10, 11
Wika S-10	0 - 3447 kPa gauge	±0.25%	2, 5
Setra 280E	0 - 1724 kPa absolute	±0.11%	1
Cole-Parmer 98072-38	60 – 110 kPa	±0.05 kPa	3-4

All pressure transducers were calibrated over the entire working pressure range and in their system position. In order to account for hysteresis error the calibration was performed by both increasing and decreasing the pressure over the calibrated range. Using the linear fit and coefficient of determination, R^2, functions in excel a minimal R^2 value of 99.9995% was established for each pressure transducer calibration data set. Factory calibration data was used for the barometric pressure transducer.

2.6.2. Differential Pressure Transducer

One differential pressure transducer was utilized in the facility for measuring the pressure drop over the desorber with factory calibration data. To maximize accuracy, a Cole-Parmer 68071-60, with a 0 to 172 kPa pressure differential range and a ±0.25% full scale accuracy, was chosen (Figure 2.33).

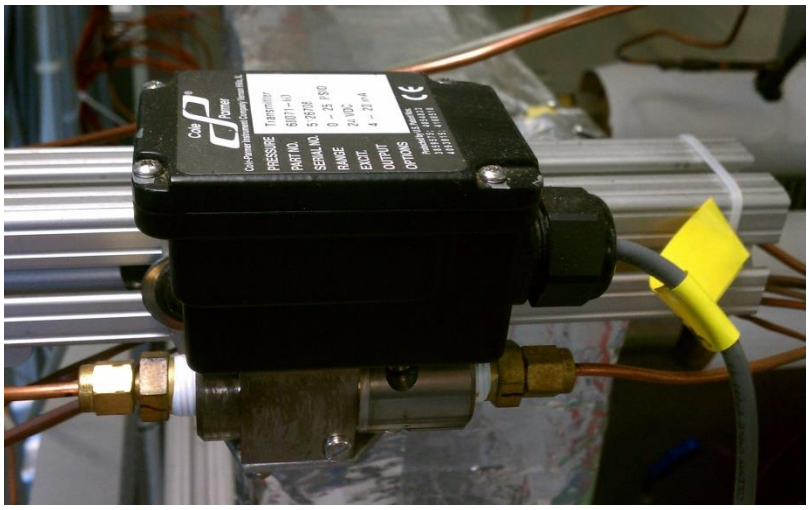

Figure 2.33: Cole-Parmer 68071-60 Differential Pressure Transducer

2.6.3. Thermocouples

In-stream and surface thermocouples were utilized throughout the facility (Figure 2.3, Figure 2.18 and Figure 2.28). All thermocouples were T-type (Figure 2.34). A temperature bath test was performed for each thermocouple before installation to validate the usage of the ±0.5°C manufacturer accuracy. Air stream temperature measurements were taken with a thermocouple grid compiled of a total of nine thermocouples, three rows, where each row measurement was consolidated, resulting in a better accuracy of ±0.3°C per row (Figure 2.35).

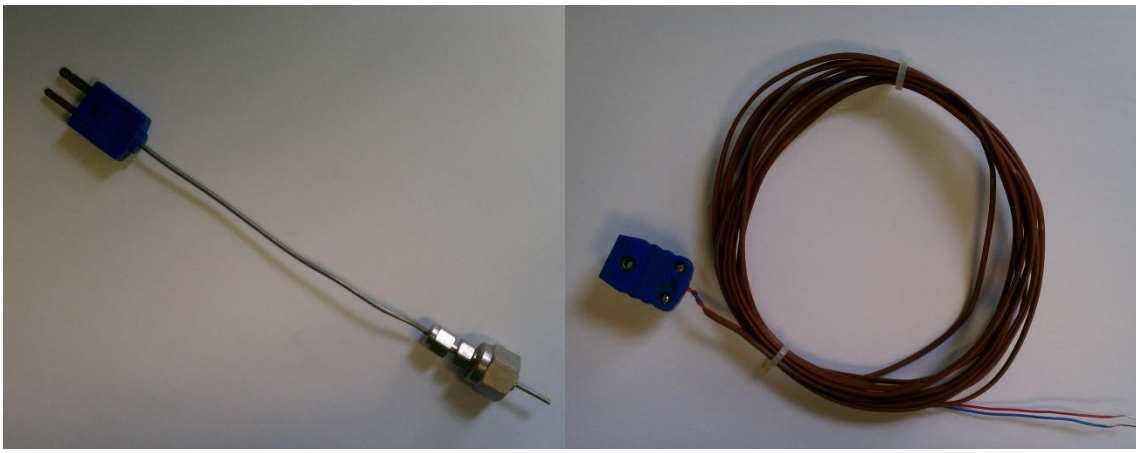

Figure 2.34: Solution and Water, In-stream and Surface T-type Thermocouples (left to right)

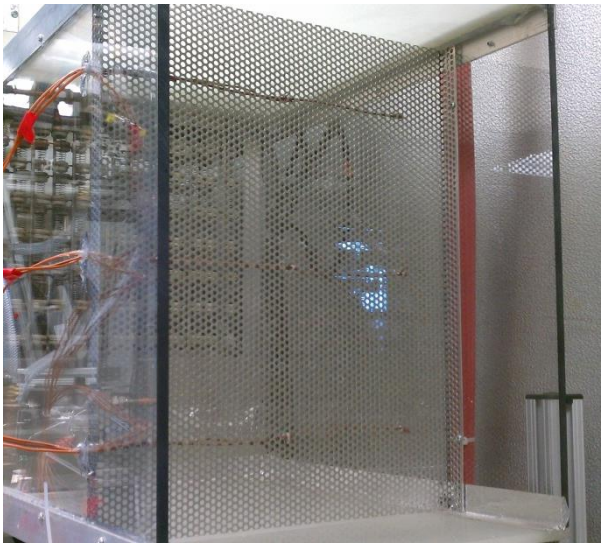

Figure 2.35: Air-stream T-type Thermocouple Grid

2.6.4. Relative Humidity Sensor

One relative humidity (RH) sensor was utilized in the wind tunnel of the facility: Testo 6651, with a 0 to 100%RH range and a ±2.5% full scale accuracy (Figure 2.36). The sensor was calibrated using three different solutions ranging over most of the relative humidity range. Using the linear fit and coefficient of determination, R^2, functions in excel a R^2 value of 99.986% was established for the calibration data set.

Figure 2.36: Testo 6651 Relative Humidity Sensor

2.6.5. Mass Flow Meters

Poor solution and refrigerant mass flow rates were measured utilizing the same mass flow meter model. For its high accuracy and two output channels ability, a Micromotion 2700R Coriolis type mass flow meter was chosen with a ±0.05% mass flow rate measurement accuracy and a fixed ±0.2 kg/m^3 density measurement accuracy (Figure 2.37). Based on mass flow rate design operating conditions, the poor solution and refrigerant mass flow meters were calibrated for a 0 to 175 g/s and 0 to 25 g/s mass flow rate range, respectively. In addition, each mass flow meter was calibrated for a 0 to 1,500 kg/m^3 density range, by repeating the manufacturer's original two-point calibration; air and water. Using the linear fit and coefficient of determination, R^2, functions in excel a R^2 value of 99.999% was established for each mass flow meter calibration data set.

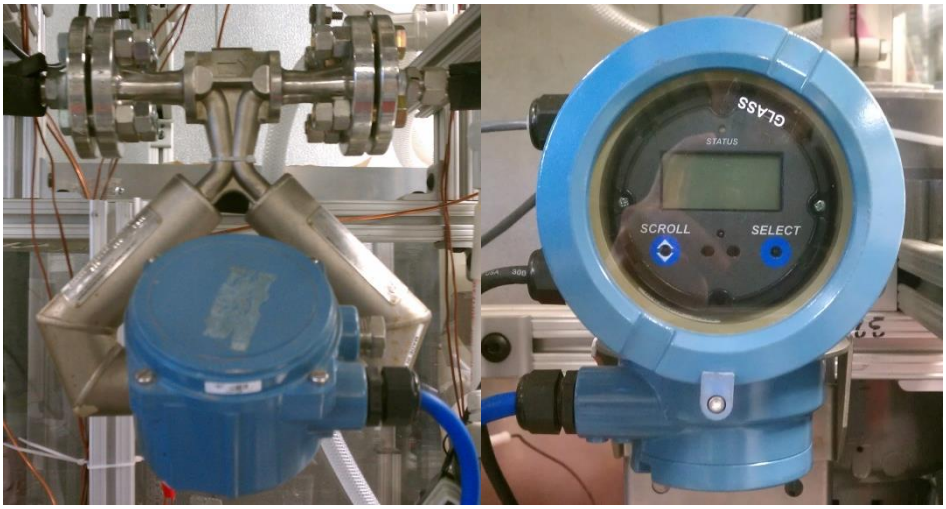

Figure 2.37: Micromotion 2700R Mass Flow Meter

2.6.6. Volume Flow Meters

Water side volumetric flow rates for both the condenser and evaporator were measured utilizing the same volume flow meter model. A Proteus PV6006SG was selected with a 1.8 to 32 LPM volumetric flow rate range and a ±1.5% full scale range accuracy, when below 50% of flow range, or a ±3% measurement accuracy, when above 50% of flow range (Figure 2.38). Factory calibration data was used for both volumetric flow meters.

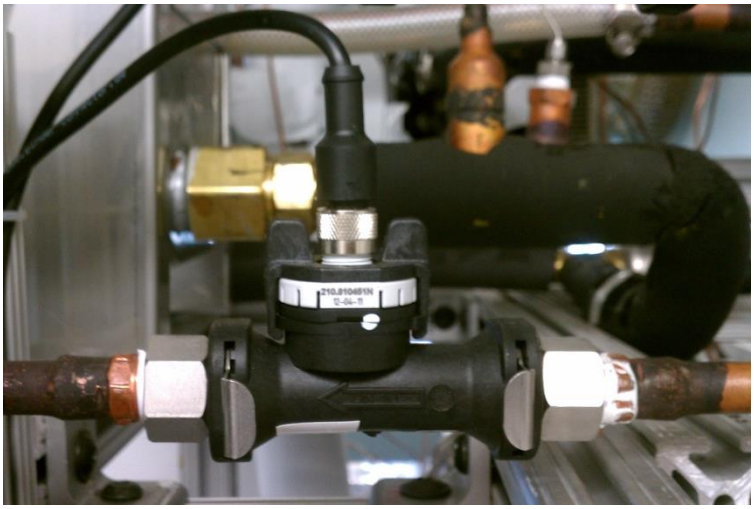

Figure 2.38: Proteus PV6006SG Volumetric Flow Meter

2.6.7. Watt Meters

Two different Ohio Semitronics, Inc. (OSI) watt meter models, GH020D and GW5020D, were utilized to measure the desorber heaters, post heaters and wind tunnel heaters power inputs (Figure 2.39). Both models have a 0 to 4 kW power range with a ±0.05% full scale range accuracy along with a ±0.2% measurement accuracy specified. Both specified accuracies were utilized and the largest value of the two was taken.

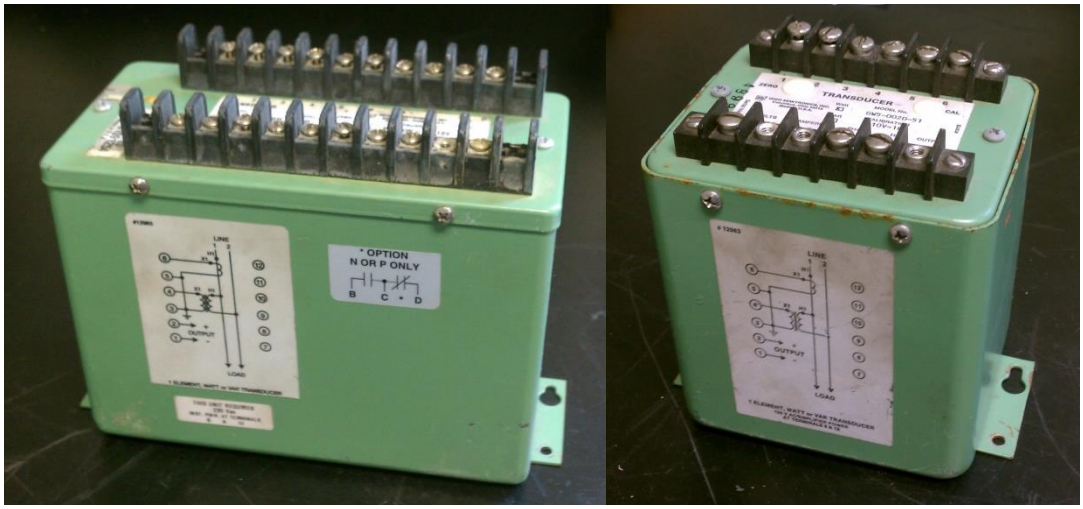

Figure 2.39: OSI GH020D/GW5020D Watt Meters

2.6.8. Liquid Level Sensor

One liquid level sensor was utilized in the facility for measuring the separator's POE32 oil level. Based on the temperature and pressure design operating conditions an Intempco LTX50 capacitance type liquid level sensor was selected, with a 15 inch probe and a ±1% full scale accuracy. The sensor was calibrated over the entire probe length and since it is a capacitance based sensor, it was done under conditions simulating the running conditions: in POE32 oil while placed in a copper tube (Figure 2.40). Using the linear fit and coefficient of determination, R^2, functions in excel a R^2 value of 99.97% was established for the calibration data set.

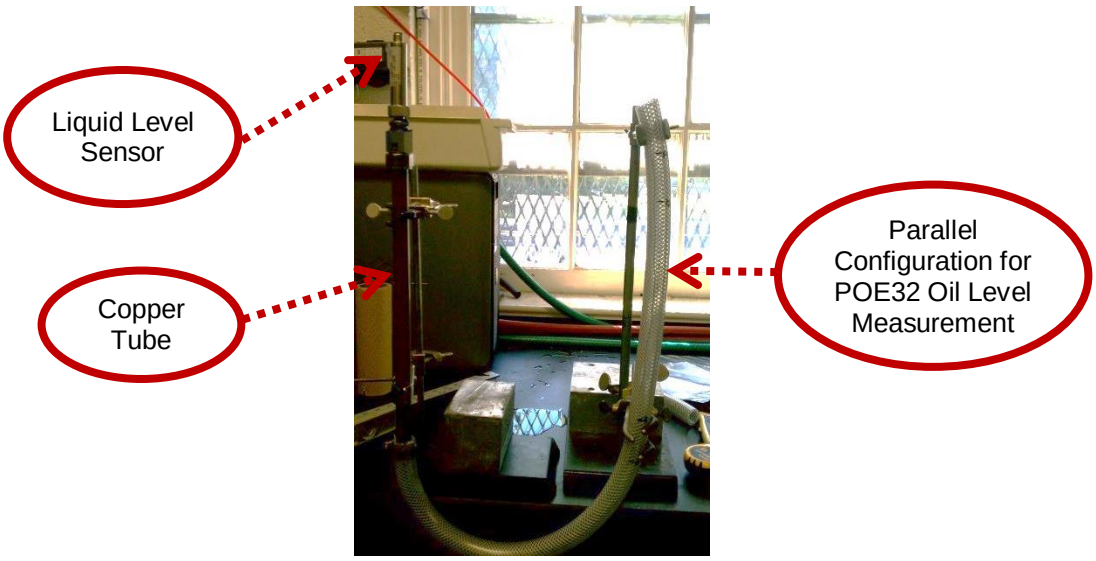

Figure 2.40: Intempco LTX50 Liquid Level Sensor

2.7. Data Acquisition System

All facility instrumentation and control devices were wired to National Instruments FieldPoint modules and fed directly into National Instruments LabVIEW program to collect the desired data, totaling in 77 incoming channels (Figure 2.41). Utilizing the incoming data channels along with XProps 2.0 [46], integrated refrigerant property routine software, system calculations were programmed and performed directly in LabVIEW. For ease of system control and monitoring during testing, LabVIEW's graphical user interface ability was utilized to display the desired live incoming system parameters and to control various system components (Figure 2.42). LabVIEW's Proportional-Integral-Derivative (PID) control ability was utilized to control multiple system components during testing, such as the pump and the wind tunnel heaters. Finally, LabVIEW was used to record all collected and calculated data for each system test run in 0.5 second intervals and output data to an Excel file for ease of data analysis.

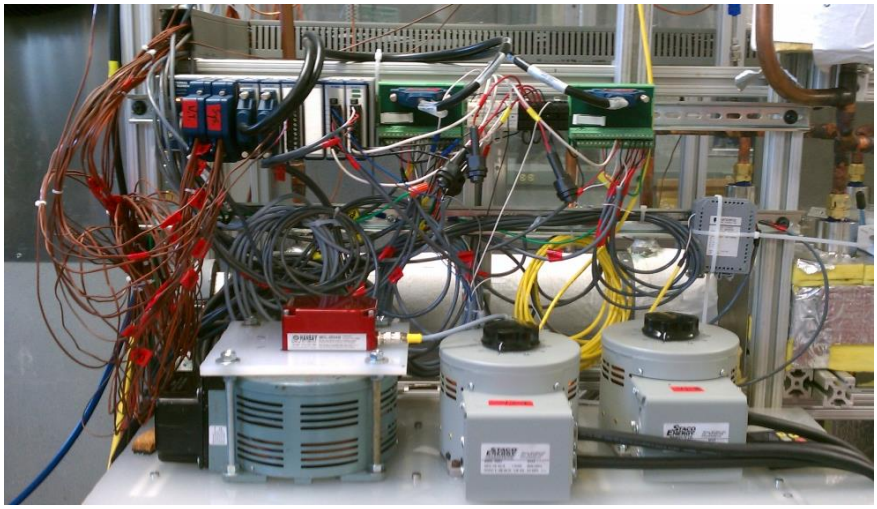

Figure 2.41: Data Acquisition Modules and Wiring

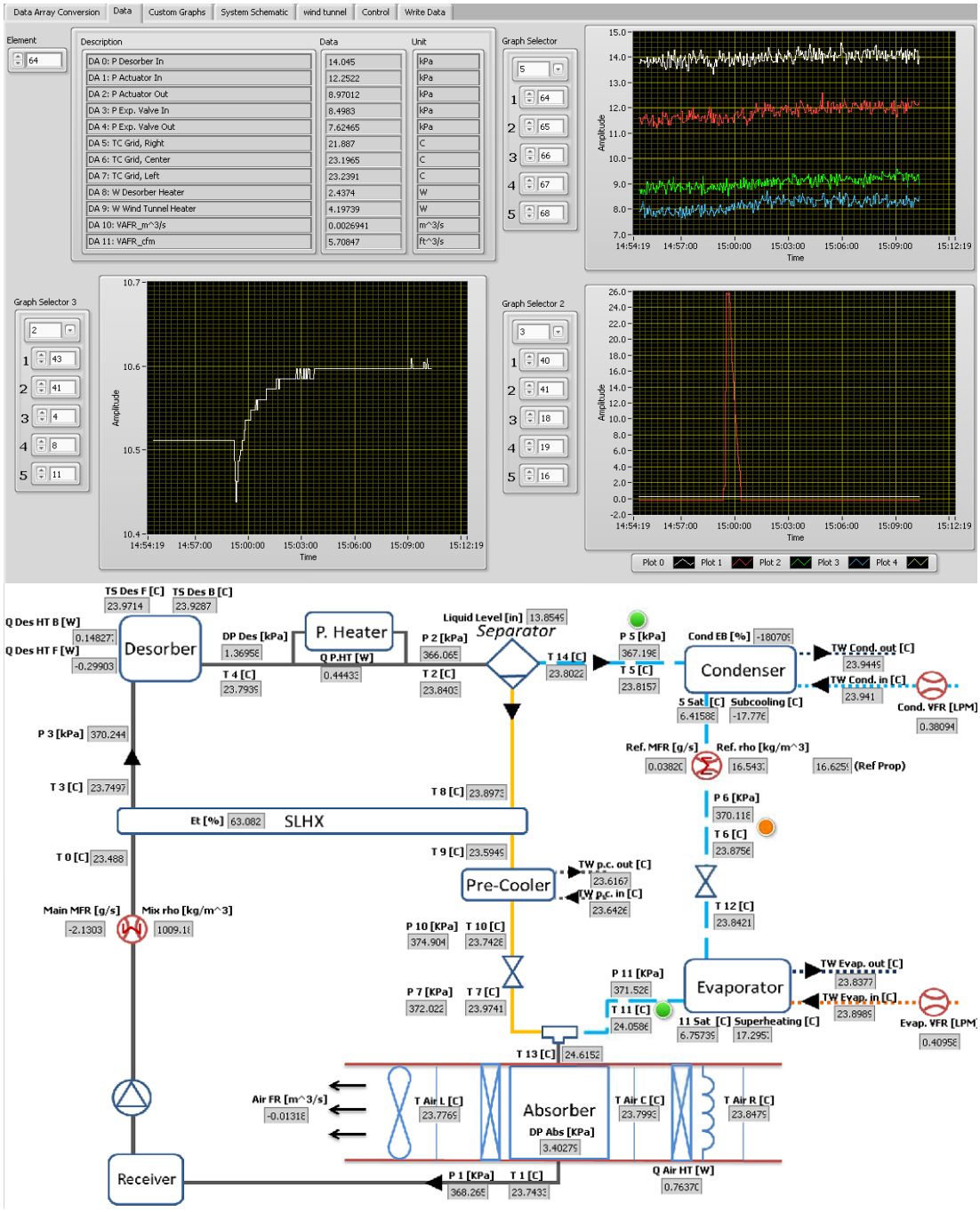

Figure 2.42: LABVIEW's Graphical User Interface

Chapter 3: Testing Procedures

In order to maintain the validity of comparing test runs to each other, testing consistency had to be maintained between each test run. To implement this required consistency along with safety reasons, startup, data collection and shutdown procedures were established and implemented throughout each test run.

3.1. System Startup Procedure

(1) Turn on Main and DAQ strip power

(2) Turn on LabVIEW and PID relay control for system heaters

(3) Start recording data at 5 second intervals

(4) Turn on room A/C and set to 25°C

(5) Turn on chiller and water heater

(6) Adjust chiller output temperature, water flow rates and water heater input capacity until water inlet condition are met (pre-cooler, condenser and evaporator)

(7) Turn on and adjust suction fan and air heaters controls for 35°C absorber inlet temperature

(8) Turn on air heaters manual switches and air heater automatic PID control

(9) Turn on pump beginning at lower mass flow rates

(10) Turn on solution heaters (desorber thin film heaters and post-heater elements) at manual switches

(11) Begin incrementally increasing pump flow rate along with solution heater inputs

(12) Turn on and manually adjust solution and R134a PID expansion valve values

- Begin decreasing solution PID value to increase solution loop ΔP
- Begin increasing R134a PID value to allow generated vapor to flow through the refrigerant loop
- Maintain separator's liquid level below 50% full throughout

(13) Adjust chiller output temperature, water flow rates and water heater input capacity as needed based on increasing solution and refrigerant loads, while maintaining desired inlet conditions

(14) Once pressure and temperature test design values have been reached, turn on automatic PID control for pump, solution and R134a expansion valves

3.2. Data Collection Procedure

Based on ASHRAE standard 37 a thirty minute data collection interval was established as the appropriate data interval for this experiment [47].

(1) Wait until system steady state is achieved

- Steady separator and receiver levels
- Steady system pressures and temperatures

(2) Set LabVIEW data recording interval to 0.5 seconds and mark the data collection starting time

(3) Monitor system for the next thirty minutes to ensure steady state is maintained

(4) At the end of data collection, return data recording to every 5 seconds

3.3. Shutdown Procedure

(1) Turn off all system heaters; solution, air and water, at manual switches and PID relay controls

(2) Reduce chiller output temperature to assist in system cooling

(3) Manually adjust pump, solution and R134a expansion valve values to maintain separator liquid level below 50%

(4) Wait until system temperatures are around 30-40°C

(5) Stop recording data

(6) Turn off Main and DAQ strip power

(7) Turn off room A/C

(8) Turn off chiller

3.4. Working Fluid Concentration Measurement Procedure

At the end of the data collection phase of chosen tests, poor and rich solution samples were taken in order to experimentally obtain dynamic R134a concentration values. These values were then compared against concentration values obtained from equilibrium data. Since these were in situ samples, the poor and rich samples had to be taken simultaneously in order to prevent data inconsistencies. Therefore, two people worked together to obtain every sample set. Some minor modifications were made for this experiment's sampling procedure since ASHRAE standard 41.4 was created for measuring low oil concentrations in a refrigerant sample, but current testing requires measuring low refrigerant concentrations in an oil sample. Once a thirty minute test was complete, the following procedure was implemented to obtain the working fluid samples:

(1) Vacuum both sample vessels

(2) Weigh both vacuumed vessels: m_{empty}

(3) Connect both vessels to the sample ports

(4) Vacuum both sample vessels once again, to vacuum the additional port connection tubes

(5) Close vessel needle valve and disconnect vacuum pump

(6) In synchronization, on the count of three, open system ball valve, open sample ball valve, close sample ball valve, close system ball valve

(7) Weigh filled vessels: $m_{mixture}$

(8) Orient the vessels vertically with needle valve facing upward

(9) Slowly and carefully open the needle valve and allow R134a to be recovered

(10) Once hissing sound stops, close the needle valve and shake the vessels

(11) Repeat steps 8 and 9 until no more R134a is recovered to atmospheric conditions

(12) Connect one vessel to the vacuum pump using a pressure gauge set as an intermediate step

- Low side to vessel
- High side leave open to atmospheric
- System side to vacuum pump

(13) Start-up vacuum pump

(14) Open, very slightly, the vessel needle valve

(15) Slowly and carefully begin closing the high pressure side until the pump stops making the loud noises associated with constant atmospheric pressure input

(16) While watching and maintaining a vacuum reading that is decreasing very slowly

- Slowly and simultaneously open the vessel needle valve while closing the gauge high side
- Once the gauge high side is completely closed, continue slowly opening the vessel needle valve

(17) Continue pulling vacuum for one hour once a minimal vacuum reading of 500 microns is achieved

(18) Close the vessel needle valve at the end of the one hour of constant vacuum reading

(19) Weigh the vessel: m_{POE32}

(20) Repeat steps 12 through 19 for the second vessel

Chapter 4: Data Analysis

The majority of data analysis was programmed and calculated directly in LabVIEW while utilizing XProps 2.0 and AProp property routines for respective R134a, water and air properties [46, 48]. XProps 2.0 is an enhancement of NIST standard reference databases (REFPROP [49]) and AProp is a LabVIEW sub-vi code utilizing ASHRAE fundamentals for air properties. Both were integrated into LabVIEW as software property routines. The remainder of calculations was programmed in Excel utilizing the Macro capabilities, unless otherwise noted.

4.1. Solution Loop Performance

Solution loop performance calculations were based on three types of direct measurements; pressure, temperature and mass flow rates. The solution heat exchanger effectiveness was calculated using the concept of energy balance, where the effectiveness is the product of the ratio between the limiting side of the heat exchanger, which can be either the hot or cold side, and the maximum possible heat transfer given the hot and cold side temperatures (Equation 9). The circulation ratio (CR) is defined as the ratio between the poor solution mass flow rate and the vapor generation mass flow rate and was calculated as such (Equation 10).

$$\varepsilon_{slhx} = \min\left(\frac{T_{cold,out} - T_{cold,in}}{T_{hot,in} - T_{cold,in}}, \frac{T_{hot,in} - T_{hot,out}}{T_{hot,in} - T_{cold,in}}\right) \quad \text{Equation 9}$$

$$CR = \frac{\dot{m}_{poor\ solution}}{\dot{m}_{vapor}} \quad \text{Equation 10}$$

The poor solution concentration was calculated using the measured vapor and poor solution mass flow rates along with the rich solution concentration determined

using CHEMCAD and its equilibrium data and Equation of State (EOS) calculations (Equation 11 through Equation 15). The poor solution concentration was also verified using an experimentally determined density correlation based on concentration and temperature (Equation 16) [50]. Where x is the mass concentration of R134a, T is the temperature of the mixture in degree kelvin and a_1 through a_9 are coefficient values obtained specifically for R134a/POE32 mixture. The poor solution concentration value was extrapolated by equating the poor solution density measurement with that of the correlation (Equation 16) and then compared to the value obtained using CHEMCAD (Equation 15) as described above.

$$\dot{m}_{rich\ solution} = \dot{m}_{poor\ solution} - \dot{m}_{vapor} \quad \text{Equation 11}$$

$$x_{rich\ solution} = f(T_8, P_8) \quad \text{Equation 12}$$

$$\dot{m}_{R,rich\ solution} = x_{rich\ solution} * \dot{m}_{rich\ solution} \quad \text{Equation 13}$$

$$\dot{m}_{R,poor\ solution} = \dot{m}_{R,rich\ solution} + \dot{m}_{vapor} \quad \text{Equation 14}$$

$$x_{poor\ solution} = \frac{\dot{m}_{R,poor\ solution}}{\dot{m}_{poor\ solution}} \quad \text{Equation 15}$$

$$\rho = a_1 + a_2 T + a_3 T^2 + x(a_4 + a_5 T + a_6 T^2) + x^2(a_7 + a_8 T + a_9 T^2) \quad \text{Equation 16}$$

4.2. <u>Desorber Performance</u>

Desorber performance calculations were based on measured thin film heat input, measured desorber inlet and outlet temperatures along with desorber geometry. The desorber effective heat flux was calculated by dividing the measured heat input by the mini-channel planform area (Equation 17, Equation 18). The desorber mean heat transfer coefficient was calculated using a fin efficiency unit cell model base on in-stream desorber temperatures, surface temperatures and desorber geometry

(Equation 19 through Equation 23) (Figure 4.1) [51]. The desorber inlet and outlet qualities were determined using CHEMCAD and its equilibrium data and Equation of State (EOS) calculations based on measured pressures and temperatures (Equation 24, Equation 25), along with solution concentration (Equation 15).

$$q''_{eff} = \frac{P_{des}}{A_p} \quad \text{Equation 17}$$

$$A_p = 2L_{ch}\left[N_{ch} * W_{ch} + (N_{ch} - 1)W_{ch,s}\right] \quad \text{Equation 18}$$

$$q''_{eff} W_{cell} = h_{mean}(T_{wall,in} - T_{avg,i})(W_{ch} + 2\eta H_{ch}) \quad \text{Equation 19}$$

$$T_{avg,i} = \frac{T_{des,out} - T_{des,in}}{2} \quad \text{Equation 20}$$

$$\eta = \frac{\tanh(mLH_{ch})}{mLH_{ch}} \quad \text{Equation 21}$$

$$mL = \sqrt{\frac{h_{mean}}{k_s W_w}} \quad \text{Equation 22}$$

$$T_{wall,in} = T_{surface} - \frac{q''_{eff} H_{w2}}{k_s} \quad \text{Equation 23}$$

$$x_{q,inlet} = f\left(x_{poor\ solution}, T_3, P_3\right) \quad \text{Equation 24}$$

$$x_{q,outlet} = f\left(x_{poor\ solution}, T_4, P_4\right) \quad \text{Equation 25}$$

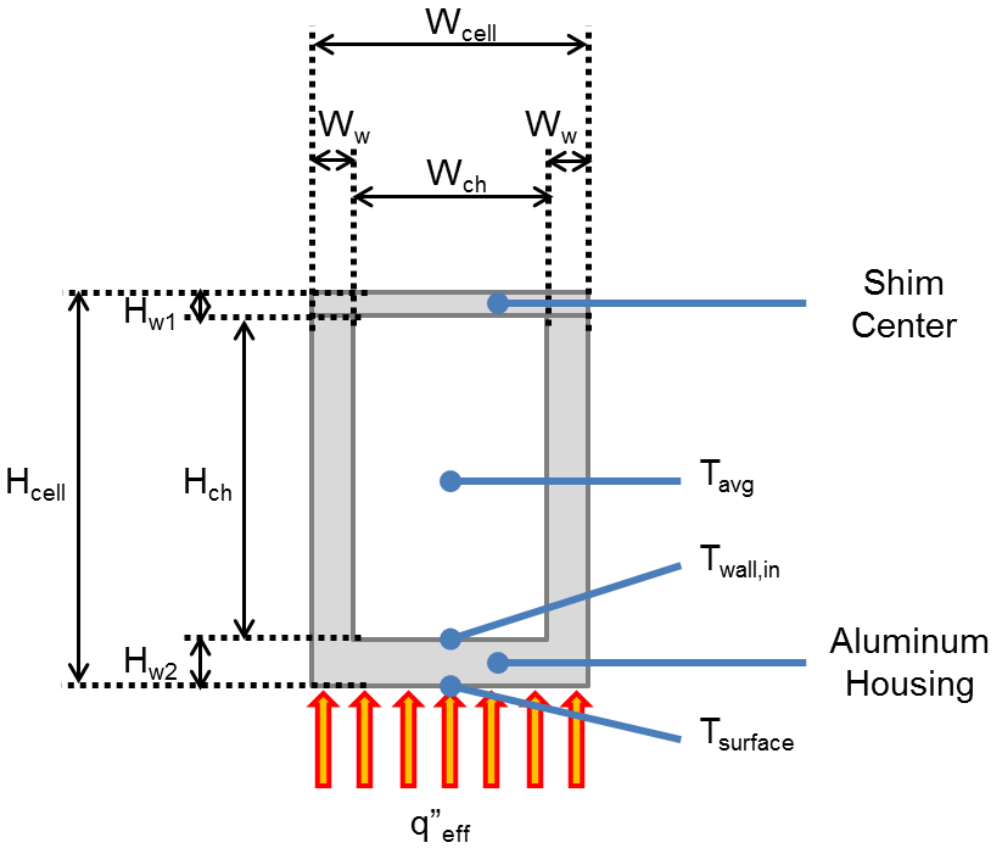

Figure 4.1: Fin Efficiency Unit Cell Model

4.3. <u>Refrigerant Loop and Water Loop Performance</u>

Refrigerant side calculations were based on the direct measurement of vapor mass flow rate, temperatures and pressures along with enthalpy property routines. The condenser heat output was calculated using the energy balance over the condenser (Equation 26 through Equation 28). The evaporator heat input was calculated in the same manner the condenser was (Equation 29 through Equation 31).

$$\dot{Q}_{R,cond} = \dot{m}_{vapor}(h_5 - h_6) \qquad \text{Equation 26}$$

$$h_5 = f(T_5, P_5) \qquad \text{Equation 27}$$

$$h_6 = f(T_6, P_6) \qquad \text{Equation 28}$$

$$\dot{Q}_{R,evap} = \dot{m}_{vapor}(h_{11} - h_{12})$$ Equation 29

$$h_{11} = f(T_{11}, P_{11})$$ Equation 30

$$h_{12} = f(T_{12}, P_{12})$$ Equation 31

Water side calculations were based on the direct measurement of volumetric flow rates and temperatures along with density and specific heat property routines. The condenser heat output was calculated using the energy balance over the condenser (Equation 32 through Equation 34). The pressure was assumed to be atmospheric pressure based on the chiller specifications and as constant due to the negligible effect a minimal pressure drop has on water density and specific heat within the operating conditions. The evaporator heat input was calculated in the same manner the condenser was (Equation 35 through Equation 37).

$$\dot{Q}_{w,cond} = \rho_{w,cond}\dot{V}_{cond}C_{p,w,cond}(T_{w,cond,out} - T_{w,cond,in})$$ Equation 32

$$\rho_{w,cond} = f(T_{avg,cond}, P_{atm})$$ Equation 33

$$C_{p,w,cond} = f(T_{avg,cond}, P_{atm})$$ Equation 34

$$\dot{Q}_{w,evap} = \rho_{w,evap}\dot{V}_{evap}C_{p,w,evap}(T_{w,evap,in} - T_{w,evap,out})$$ Equation 35

$$\rho_{w,evap} = f(T_{avg,evap}, P_{atm})$$ Equation 36

$$C_{p,w,evap} = f(T_{avg,evap}, P_{atm})$$ Equation 37

Once both refrigerant-side and water-side condenser and evaporator capacities were calculated their respective energy balances were calculated (Equation 38, Equation 39).

$$EB_{cond} = 100 * \frac{\dot{Q}_{w,cond}}{\dot{Q}_{R,cond}}$$ Equation 38

$$EB_{evap} = 100 * \frac{\dot{Q}_{w,evap}}{\dot{Q}_{R,evap}} \quad \text{Equation 39}$$

4.4. Air-Side Performance

Air side calculations were based on four measurement types: three thermocouple grid temperatures, relative humidity, barometric pressure and the heater power input. The pressure throughout the wind tunnel was assumed to be atmospheric pressure and constant due to the negligible pressure drop of 0.32 kPa calculated at the maximum air flow rate of 0.448 m^3/s. The volumetric air flow rate was calculated using the energy balance over the wind tunnel heater (Equation 40 through Equation 43). Each thermocouple grid temperature was the average value of its three rows (Equation 41). The density and specific heat of air were obtained using property routines (Equation 42, Equation 43). The temperature difference was between the center and right wind tunnel thermocouple grids, while the heat input was that of the wind tunnel heater measured by a watt meter. Once the volumetric air flow rate was calculated the absorber heat output was calculated using the air side energy balance over the absorber (Equation 40 through Equation 44). This time the temperature difference was between the left and center wind tunnel thermocouple grid, while the volumetric flow rate was the one just calculated (Equation 40).

$$\dot{V}_{air} = \frac{\dot{Q}_{heater}}{\rho_{air} C_{p,air} (T_{grid,c} - T_{grid,r})} \quad \text{Equation 40}$$

$$T_{grid} = \frac{T_{top} + T_{center} + T_{bottom}}{3} \quad \text{Equation 41}$$

$$\rho_{air} = f(T, P, RH) \quad \text{Equation 42}$$

$$C_{p,air} = f(T, P, RH)$$ Equation 43

$$\dot{Q}_{abs} = \rho_{air}\dot{V}_{air}C_{p,air}(T_{grid,l} - T_{grid,c})$$ Equation 44

4.5. Uncertainty Analysis

Uncertainty analysis was conducted on all measured and calculated data. Both measured and calculated variables have systematic and random uncertainty components. The systematic uncertainty, u_{sys}, for a measured variable is the accuracy of the measuring device (Table 4), while the systematic uncertainty for a calculated variable is derived from the Pythagorean summation of uncertainties (Equation 45). Where u_n is the systematic uncertainty of each measured parameters and $\frac{\partial f}{\partial x_n}$ is the partial derivative of the calculated parameter, f, relative to each measured parameter, x_n.

Table 4: Systematic Uncertainties of Measured Parameters

Parameter	Accuracy
Pressure (Setra C206)	±0.13% FS
Pressure (Wika S-10)	±0.25% FS
Pressure (Setra 280E)	±0.11% FS
Pressure (Cole-Parmer 98072-38)	±0.05 kPa
Differential Pressure (Cole-Parmer 68071-60)	±0.25% FS
Temperature (Omega TT-T-20SLE)	±0.5°C
Relative Humidity (Testo 6650)	±2.5% FS
Mass Flow Rate (Micromotion 2700R)	±0.05% Value
Density (Micromotion 2700R)	±0.2 kg/m^3
Volumetric Flow Rate (Proteus PV6006SG)	±1.5% FS /±3% Value
Power (Ohio Semitronics GW020D, GW5020D)	±0.05% FS/±0.2% Value
Liquid Level (Intempco LTX50)	±1% FS

Random uncertainty, u_{rand}, is the standard deviation of the actual measurements collected over a certain time interval (Equation 46). Where x_j is the measured variable data point, $\bar{x}$ is the measured variable average over the entire data set and N is the number of data points in the collected data set. The total uncertainty, u_t, is the summation of the two (Equation 47). A sample data set of a typical test run can be seen in Table 5.

$$u_{sys} = \sqrt{\left(u_1 * \frac{\partial f}{\partial x_1}\right)^2 + \left(u_2 * \frac{\partial f}{\partial x_2}\right)^2 + \cdots + \left(u_n * \frac{\partial f}{\partial x_n}\right)^2} \quad \text{Equation 45}$$

$$u_{rand} = \sqrt{\frac{\sum\left(x_j - \bar{x}\right)^2}{N - 1}} \quad \text{Equation 46}$$

$$u_t = u_{sys} + u_{rand} \quad \text{Equation 47}$$

Table 5: Sample Uncertainty Analysis

System Parameter (Figure 2.3**)**	**Unit**	**Average Value**	**Total Uncertainty**	**% Error**
P2	kPa	1602	9.98	0.62
P7	kPa	656.0	6.51	0.99
P11	kPa	651.3	6.42	0.99
T2	°C	150.3	0.79	0.53
T7	°C	43.54	0.60	1.37
MFR Pump	g/s	69.3	0.13	0.19
MFR R134a	g/s	5.00	0.01	0.28
VFR Condenser	LPM	3.00	0.50	16.8
VFR Evaporator	LPM	6.97	0.50	7.13
Air-Side Heater Input	W	3,196	38.3	1.20
Desorber Heat Input	W	1,613	5.94	0.37
Post-Heater Input	W	3,378	54.8	1.62
Condenser Capacity - water side	W	1,240	4.56	0.37
Condenser Capacity - R134a side	W	1,218	6.93	0.57
Circulation Ratio	-	13.9	0.05	0.34
EB - Condenser	%	1.80	-	0.67
Mean Heat Transfer Coefficient	W/m^2K	2471	172.2	6.97

Chapter 5: Results and Discussion

During system testing various system parameters were varied, such as solution flow rate, desorption temperatures and pressures and rich solution absorber inlet temperature. These parameters were varied in order to investigate their effects on desorber and system heat and mass transfer performance. Once system levels stabilized; separator and receiver levels along with system temperatures and pressures, steady state data was recorded and collected for thirty minute intervals. The test matrix for the current investigation is presented in Table 6.

Table 6: Test Matrix

Low Side Pressure [kPa]	High Side Pressure [kPa]	Mass Flow Rate [g/s]	High Side Temperature [°C]
450, 600	1,300	52	120, 135, 150
		100	120, 135, 150
		140	120, 135, 150
	1,450	52	120, 135, 150
		100	120, 135, 150
		140	120, 135, 150
	1,600	52	120, 135, 150
		100	120, 135, 150
		140	120, 135, 150

5.1. Desorption Performance

5.1.1. Desorption Temperature Effect

The desorption outlet temperature was varied over the initial design matrix (Table 6). The effect of this variance on the system's circulation ratio at different outlet desorption pressures is visualized in Figure 5.1 and Figure 5.2 for poor solution flow rates of 53.4 g/s and 69.6 g/s, respectively. Higher temperatures enhance heat and mass transfer, therefore increasing vapor generation. At constant pressure, as desorption temperature increases the liquid solubility concentration decreases, therefore increasing vapor generation. The same solution flow rate is utilized for higher desorption rates, therefore decreasing the circulation ratio (Figure 5.1 and Figure 5.2).

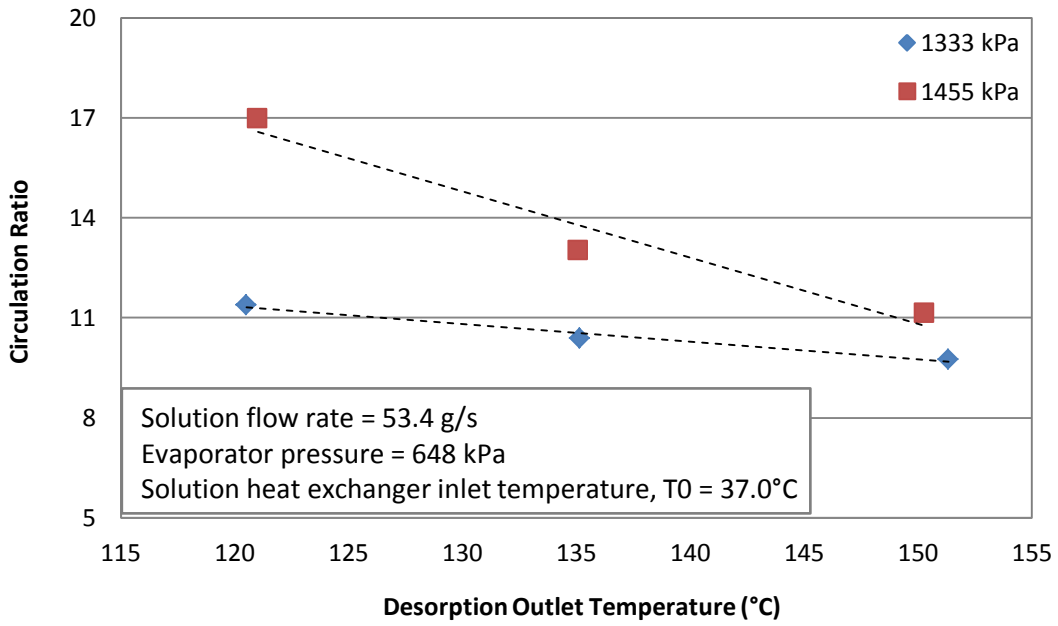

Figure 5.1: Circulation Ratio as a Function of Desorber Outlet Temperature at 53.4 g/s Poor Solution Mass Flow Rate

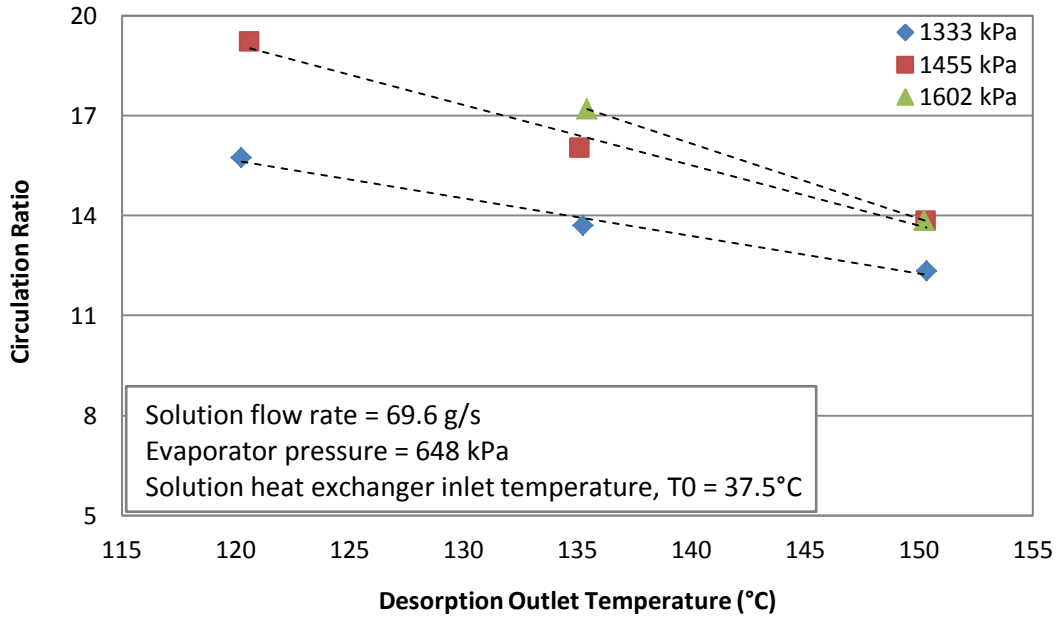

Figure 5.2: Circulation Ratio as a Function of Desorber Outlet Temperature at 69.6 g/s Poor Solution Mass Flow Rate

5.1.2. Desorption Pressure Effect

The desorption outlet pressure was varied over the initial design matrix (Table 6). The effect of this variance on vapor generation at different outlet desorption temperatures is visualized in Figure 5.3 and Figure 5.4 for poor solution flow rates of 53.4 g/s and 69.6 g/s, respectively. Lower pressures promote vapor generation. At constant temperature, as desorption pressure decreases the liquid solubility concentration decreases, therefore increasing vapor generation (Figure 5.3 and Figure 5.4). At these lower pressures, the same solution flow rate is utilized for higher desorption rates, therefore the circulation ratio decreases.

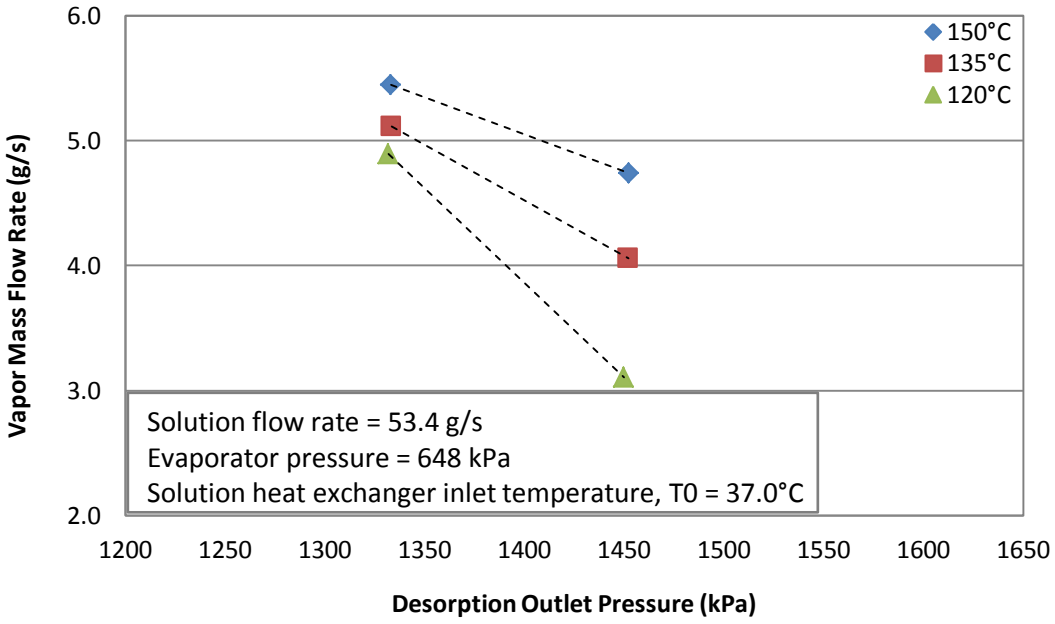

Figure 5.3: Vapor Generation as a Function of Desorber Outlet Pressure at 53.4g/s Poor Solution Mass Flow Rate

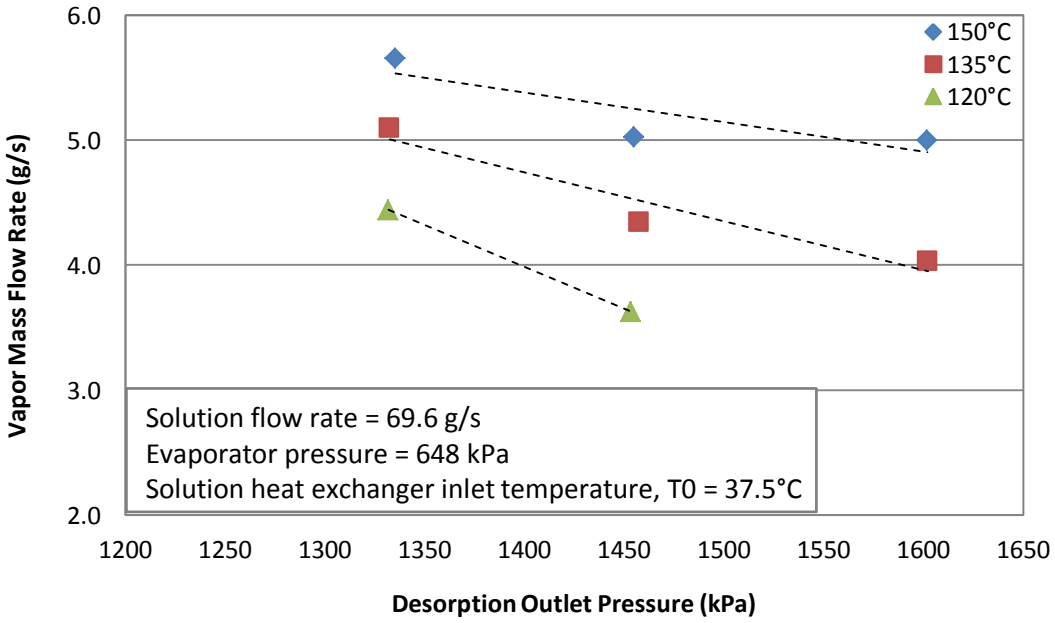

Figure 5.4: Vapor Generation as a Function of Desorber Outlet Pressure at 69.6g/s Poor Solution Mass Flow Rate

5.1.3. Density Correlation

Certain deviations from expected trends were further explored using an experimentally developed density correlation to investigate the presence of POE32 in the refrigerant loop (Equation 16). At a constant desorption temperature and solution flow rate, an increase in desorption pressure should result in a decrease in vapor generation. Therefore, an increase in circulation ratio is also expected. Yet the increase from approximately 1,450 kPa to 1,600 kPa did not produce these expected results (Figure 5.2 and Figure 5.4). Utilizing the density correlation (Equation 16) resulting POE32 concentrations of 20 to 35% were established in the refrigerant loop. The POE32 concentrations exhibited an increase in value with an increase in poor solution mass flow rate and an even greater increase with an increase in desorption pressures (Figure 5.5).

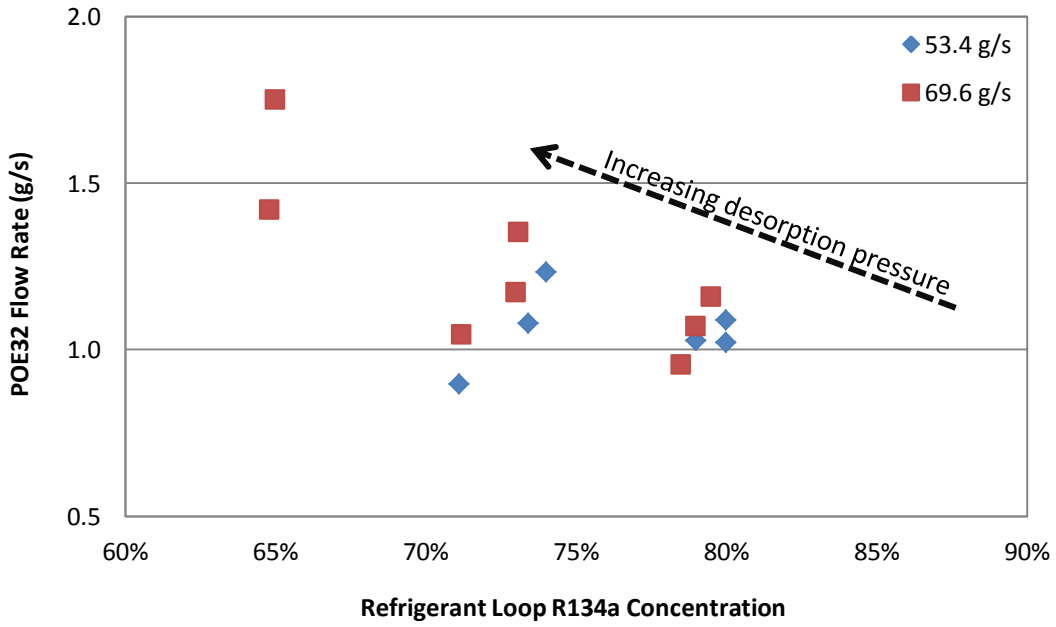

Figure 5.5: POE32 Refrigerant Loop Mass Flow Rate

Under the assumption that these POE32 concentrations were good approximations, the R134a vapor generation and circulation ratio values were recalculated utilizing the new resulting R134a refrigerant loop concentrations. The updated data fully reflected the expected trends discussed above (Figure 5.6 and Figure 5.7).

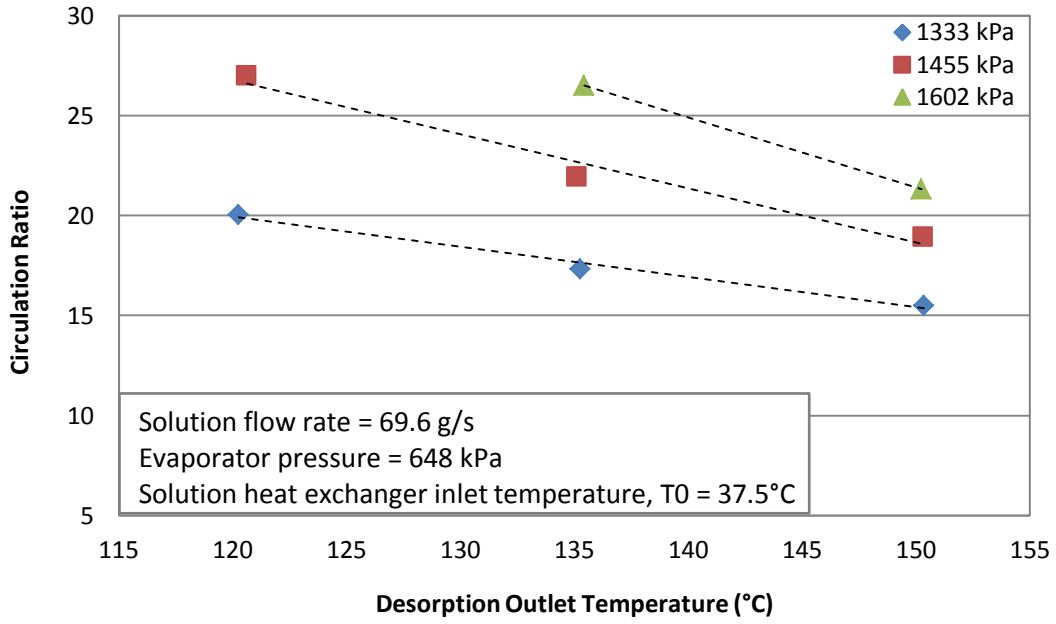

Figure 5.6: Circulation Ratio as a Function of Desorber Outlet Temperature at 69.6 g/s Poor Solution Mass Flow Rate with Adjusted R134a Concentration

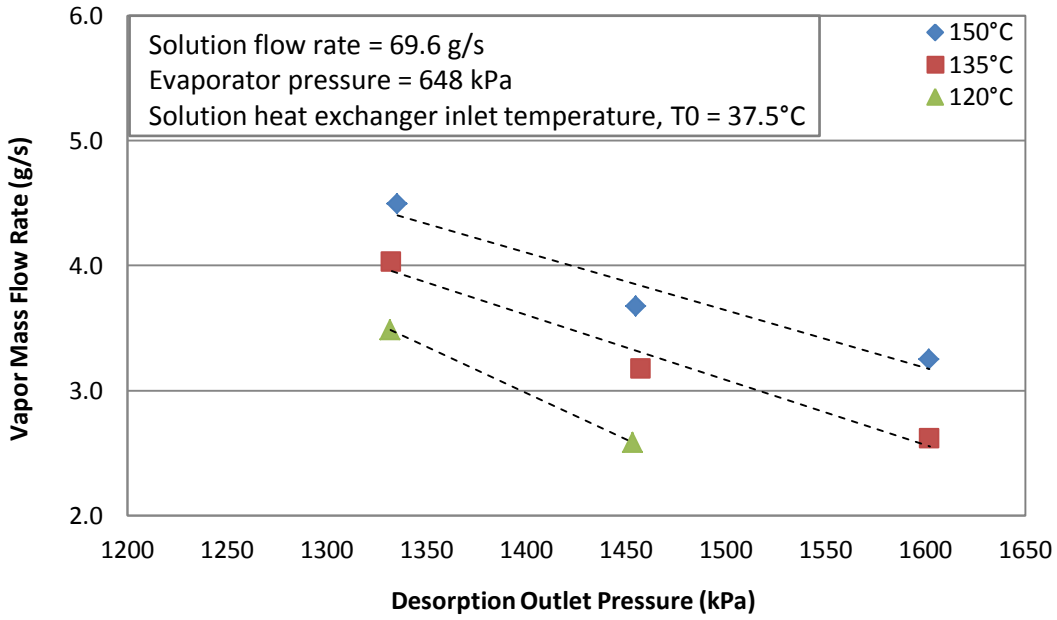

Figure 5.7: Vapor Generation as a Function of Desorber Outlet Pressure at 69.6g/s Poor Solution Mass Flow Rate with Adjusted R134a Concentration

5.1.4. Refrigerant Concentration Effect

To investigate the effect of refrigerant charge, the total system refrigerant concentration, $\frac{R134a}{R134a+POE32}$, was varied from 19.2% to 23.3%. The effect of this variance on circulation ratio at different outlet desorption temperatures is visualized in Figure 5.8. The higher system refrigerant concentration contributed to low POE32 refrigerant loop concentrations, 6% or below, in the new respective runs. Therefore, the majority of the system's POE32 charge was appropriately located in the solution loop, increasing the refrigerant absorption capacity at the absorber under the same conditions, therefore increasing poor solution concentration and possible vapor generation. The same solution flow rate is utilized for higher desorption rates, therefore decreasing the circulation ratio (Figure 5.8). This reflects the importance of

optimized refrigerant charge selection without overcharging the system, which varies from system to system due to component and therefore system volumetric changes.

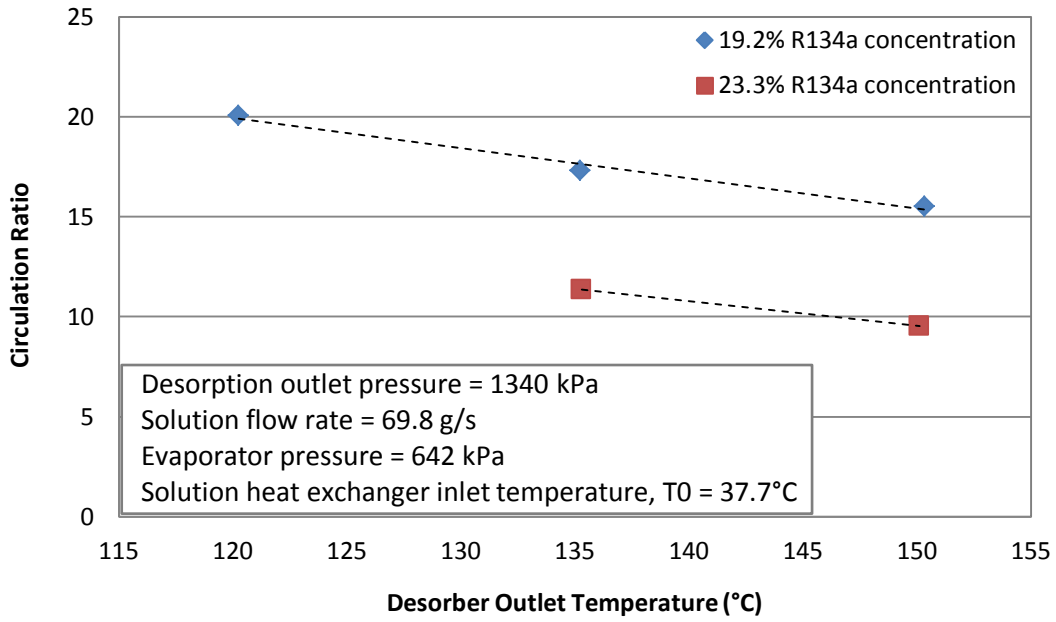

Figure 5.8: Circulation Ratio as a Function of Refrigerant System Concentration

5.1.5. Absorption Pressure and Temperature Effects

Preliminary system testing revealed the dominance of absorption pressures and temperatures over those of desorption for vapor generation limitation. At constant temperature, pressure acts as the compression driving force, compressing more refrigerant at higher pressures while liberating more refrigerant at lower pressures. At constant pressure, temperature acts as the compression driving force, liberating more refrigerant at higher temperatures while compressing more refrigerant at lower temperatures. Based on these absorption desorption phenomena, desorption favors lower pressure and higher temperature combinations, while absorption favors higher pressure and lower temperature combinations.

Initial system runs showed favorable absorption pressures overpowered desorption pressure changes. For example, under constant temperature and solution mass flow rate conditions, an increase of 60.8 kPa on the absorption end positively overpowered an increase of 195 kPa on the desorption end, therefore increasing vapor generation and decreasing circulation ratio although the desorption change should have produced the opposite effect (Figure 5.9). Confirmation of this trend over various runs concluded that the original maximum absorption pressure of 600 kPa would not be viable for further desorption testing due to major vapor generation restrictions, below 2 g/s. Therefore, the original absorption pressure upper limit was raised to 650 kPa and the initial design matrix (Table 6) was limited to that pressure.

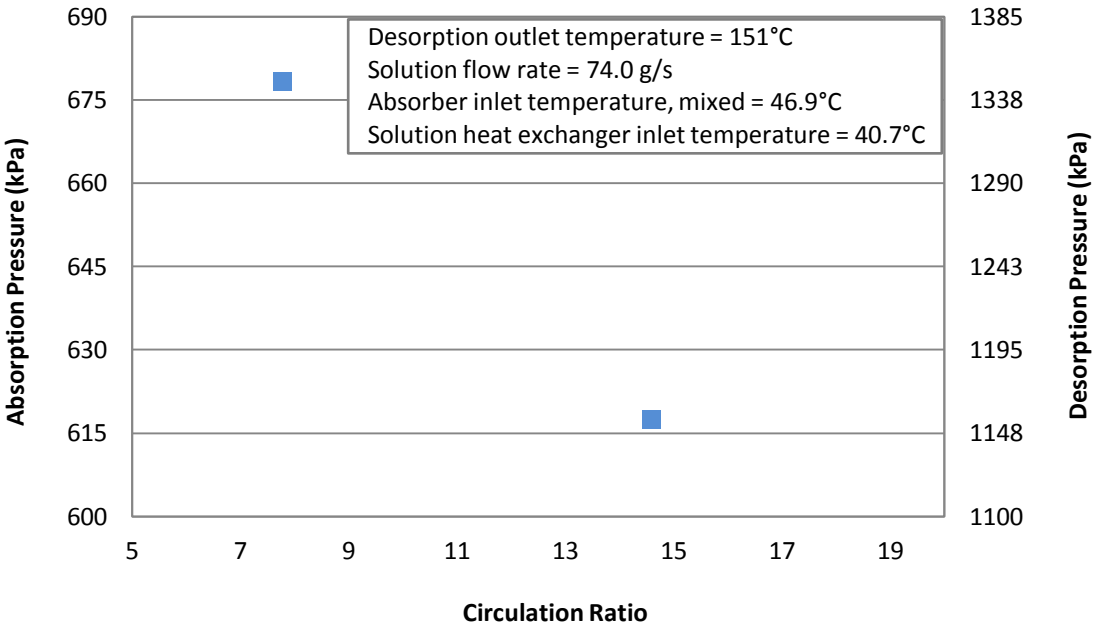

Figure 5.9: Absorption versus Desorption Pressure Effect

Further system runs reflected the absorption temperature dominance over system performance due to solubility limitations. Mixture solubility dictates that at constant pressure a decrease in temperature will allow the poor solution to absorb

more refrigerant, thereby increasing the vapor generation potential on the desorber end. Therefore, vapor generation downstream at the desorber is heavily affected by the absorber performance. Comparison of various sample runs against the T-x diagram (theoretical values based on CHEMCAD's vapor liquid equilibrium data) reveals that runs are indeed close to the solubility limitations (Figure 5.10). Deviations from being on the actual solubility curve are assumed to be intrinsically related to the differences between equilibrium data and a dynamic system, which is realistically not going to be at perfect equilibrium, therefore requiring some degrees of sub-cooling for the same concentration value.

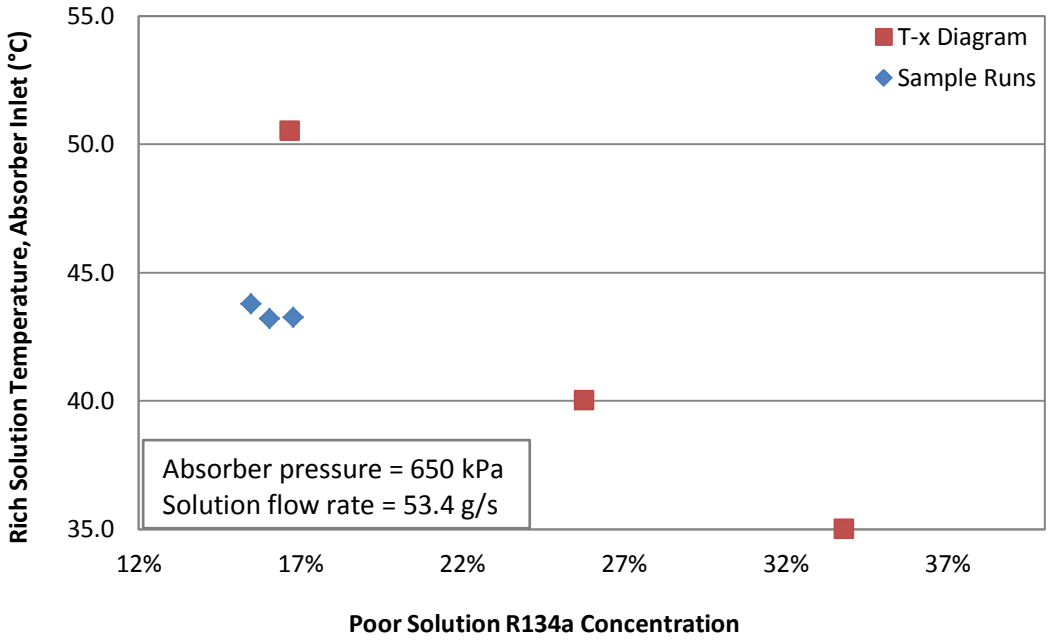

Figure 5.10: Absorber Solubility Limitation

5.1.6. Solution Flow Rate Effect

Initial system runs revealed a heat input capacity limitation. Therefore, the original poor solution mass flow rate range was downscaled to rates at which the

entire desorption outlet temperature range, 120 to 150°C, can still be achieved and the initial design matrix (Table 6) was limited to the range of 52 g/s to 70 g/s. The poor solution mass flow rate was tested at 53.4 g/s and 69.8 g/s. The effect of this variance on vapor generation and circulation ratio at constant pressure is visualized in Figure 5.11 and Figure 5.12, respectively. Higher solution mass flow rates enhance heat and mass transfer, therefore increasing vapor generation (Figure 5.11). Although higher mass flow rates require higher heat input to achieve the same outlet temperature. At the same time, the benefit of increased vapor generation is overshadowed by the incrementally larger increase on the solution side flow rate, resulting in higher circulation ratios (Figure 5.12).

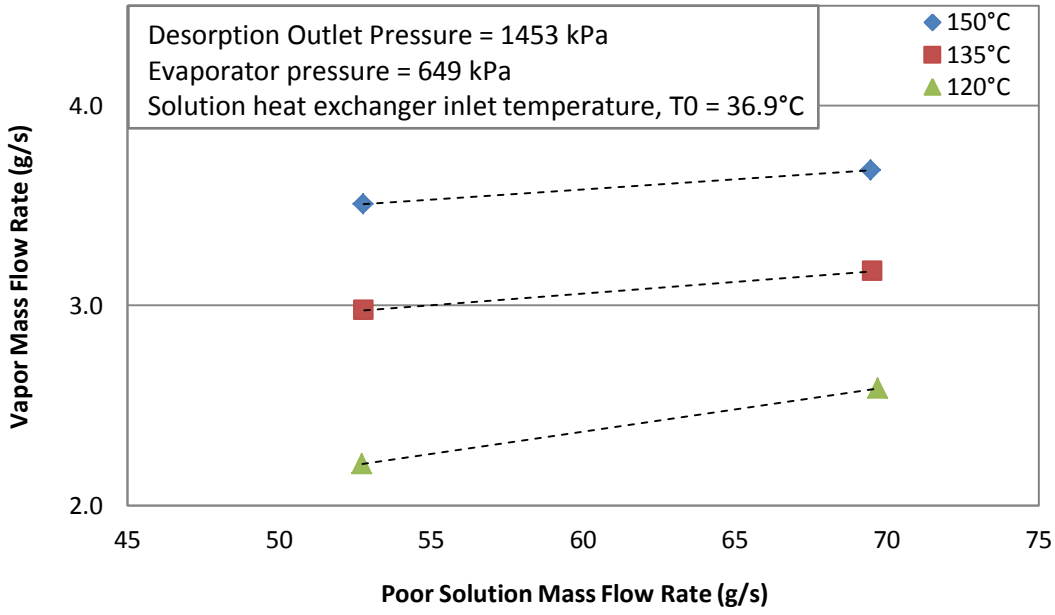

Figure 5.11: Vapor Generation as a Function of Poor Solution Mass Flow Rate at Constant Pressure

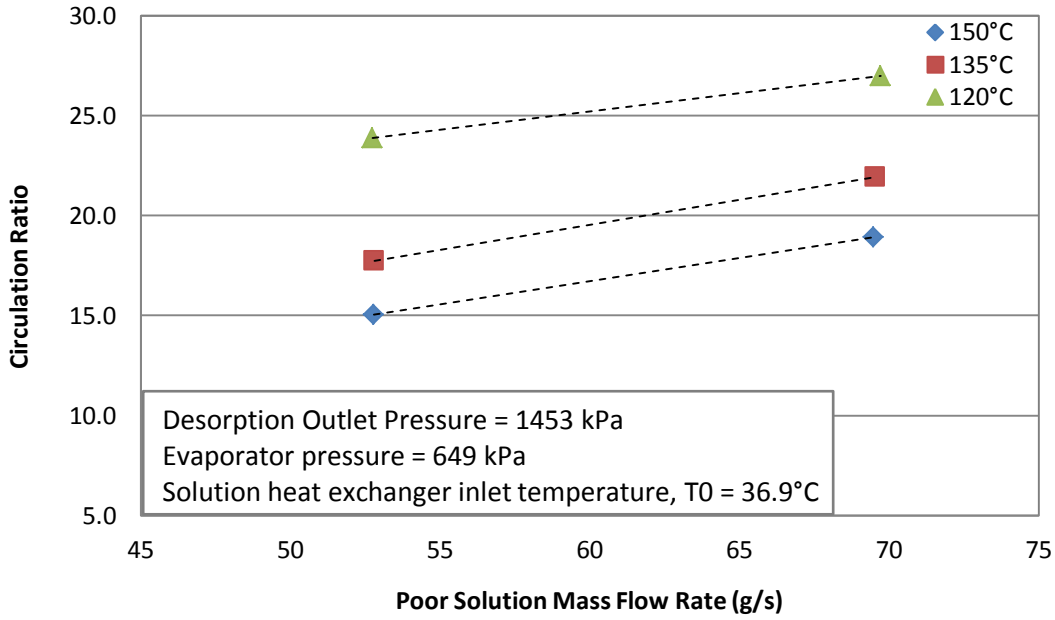

Figure 5.12: Circulation Ratio as a Function of Poor Solution Mass Flow Rate at Constant Pressure

As mention above, higher solution mass flow rates enhance heat and mass transfer, therefore increasing vapor generation. At constant pressures, higher flow rates should enhance the poor solution refrigerant concentration, which is the cause for the higher vapor generation rates, as the mass transfer increases at the absorber end. A poorer solution contains more refrigerant per unit mass, therefore decreasing circulation ratios as the desorber has higher vapor generation capacity per unit mass, at the same pressure. A reversal of the circulation ratio trend was reflected in Figure 5.12, where the circulation ratio increased with poor solution mass flow rate. The cause of this trend reversal is reflected in Figure 5.13, where the poor solution R134a concentration decreases as the poor solution mass flow rate increases. Therefore, concluding that the concentration ratio trend reversal is a product of absorber performance limitations previously mentioned.

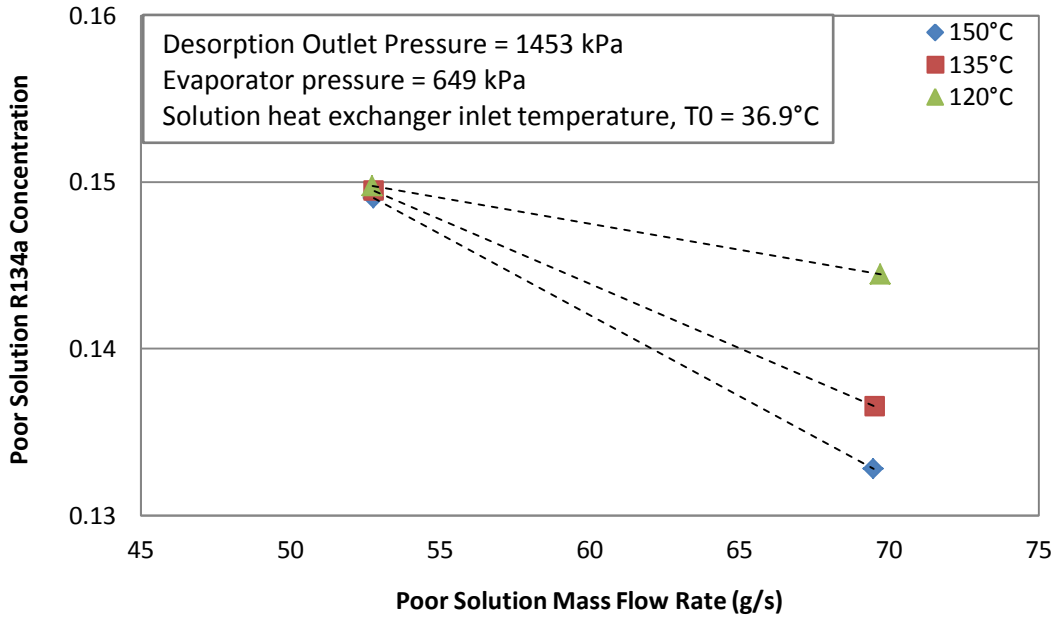

Figure 5.13: Poor Solution R134a Concentration as a Function of Poor Solution Mass Flow Rate at Constant Pressure

The effect of the same solution mass flow rate variance on vapor generation and circulation ratio at constant temperature is visualized in Figure 5.14 and Figure 5.15, respectively. For the same reasons discussed above, an increase in solution mass flow rate increases vapor generation, while exhibiting a reverse trend of increased circulation ratios. On the other hand, expected vapor generation and circulation ratios trends were observed due to pressure variation. At a constant temperature as desorption pressure decreases the liquid solubility concentration decreases, therefore increasing vapor generation (Figure 5.14). At these lower pressures, the same solution flow rate is utilized for higher desorption rates, therefore the circulation ratio decreases (Figure 5.15).

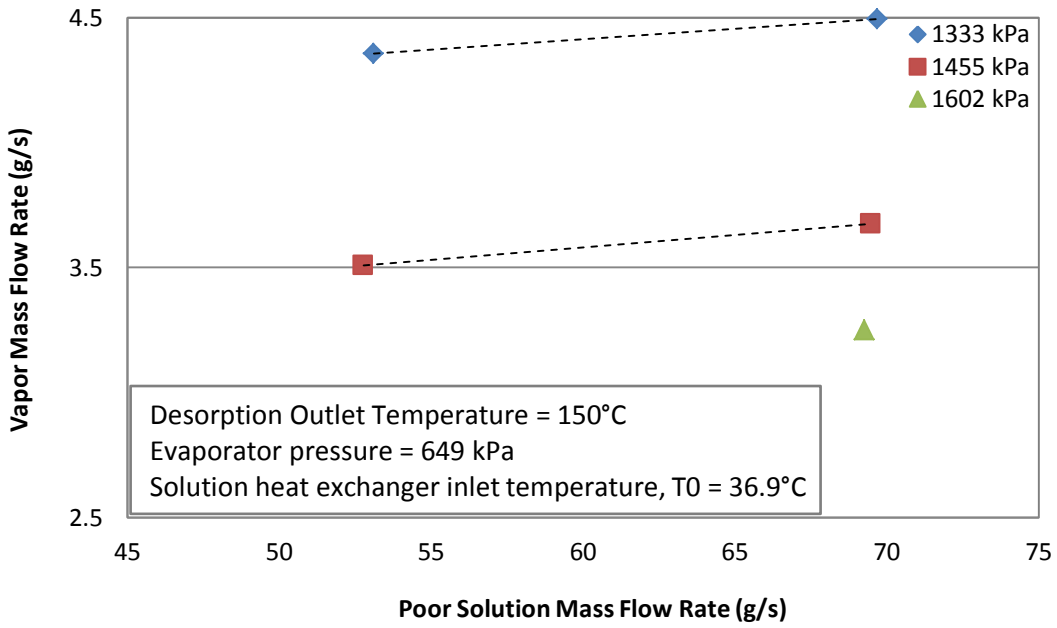

Figure 5.14: Vapor Generation as a Function of Poor Solution Mass Flow Rate at Constant Temperature

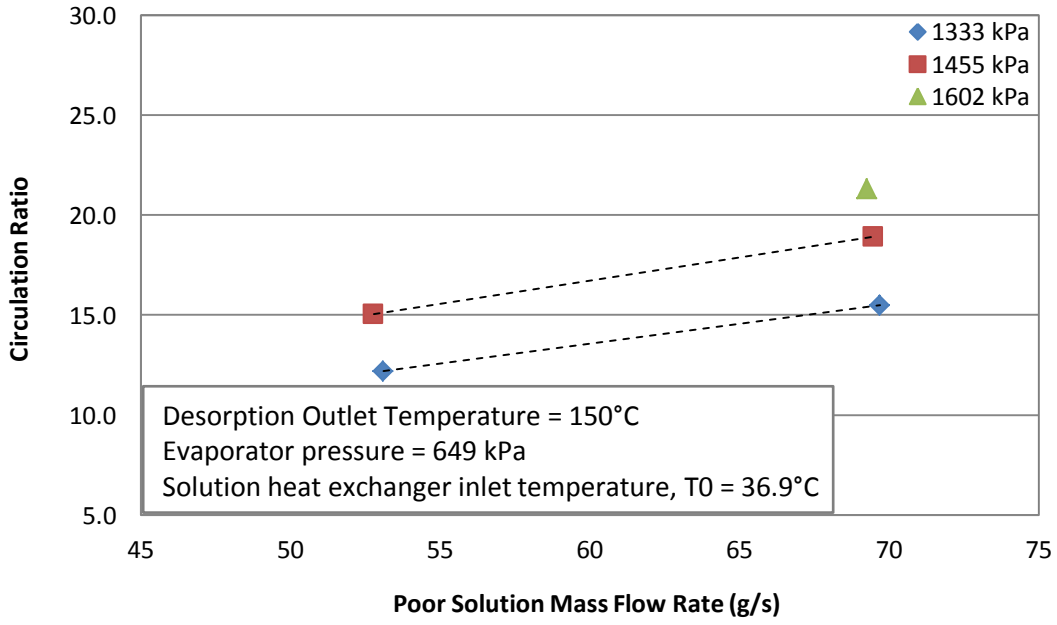

Figure 5.15: Circulation Ratio as a Function of Poor Solution Mass Flow Rate at Constant Temperature

5.2. *Desorber Performance*

5.2.1. Mean Heat Transfer Performance

A mini-channel desorber was investigated for the benefits of enhanced heat and mass transfer while utilizing a smaller design. Higher temperatures and poor solution mass flow rates enhance heat and mass transfer, therefore increasing vapor generation in the two-phase solution mixture. At a constant pressure, as higher temperatures are applied the mean heat transfer coefficient increases as expected in the two-phase mixture (Figure 5.16 and Figure 5.17). At a constant temperature, decreasing pressure increases the mean heat transfer coefficient, as lower pressure promotes vapor generation (Figure 5.16). At a constant temperature, increasing poor solution mass flow rate increases the mean heat transfer coefficient, as higher mass flow rate promotes heat and mass transfer (Figure 5.17).

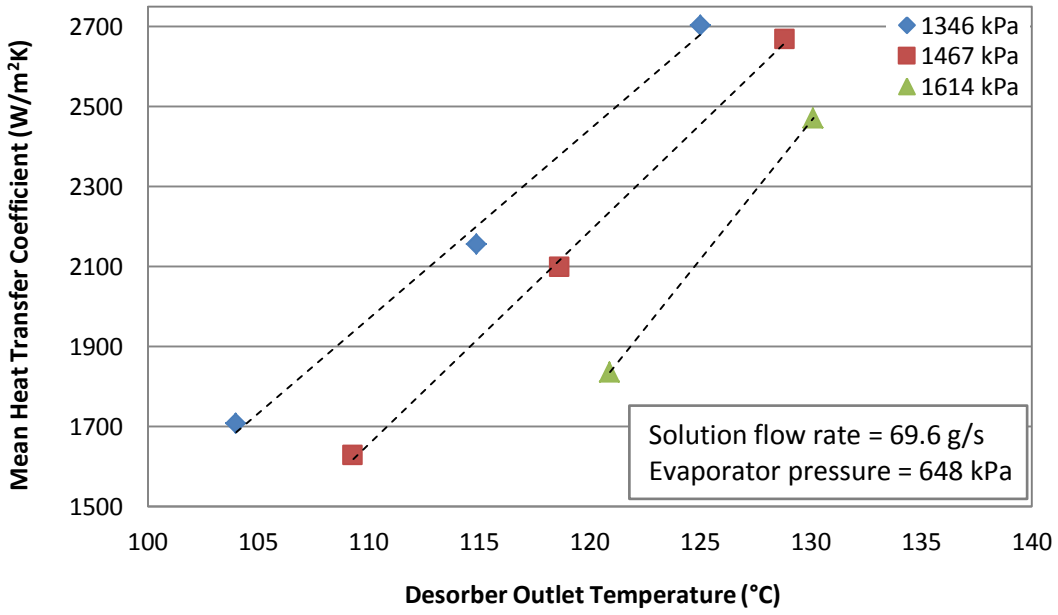

Figure 5.16: Mean Heat Transfer Coefficient as a Function of Desorber Outlet Temperature at Constant Poor Solution Mass Flow Rate

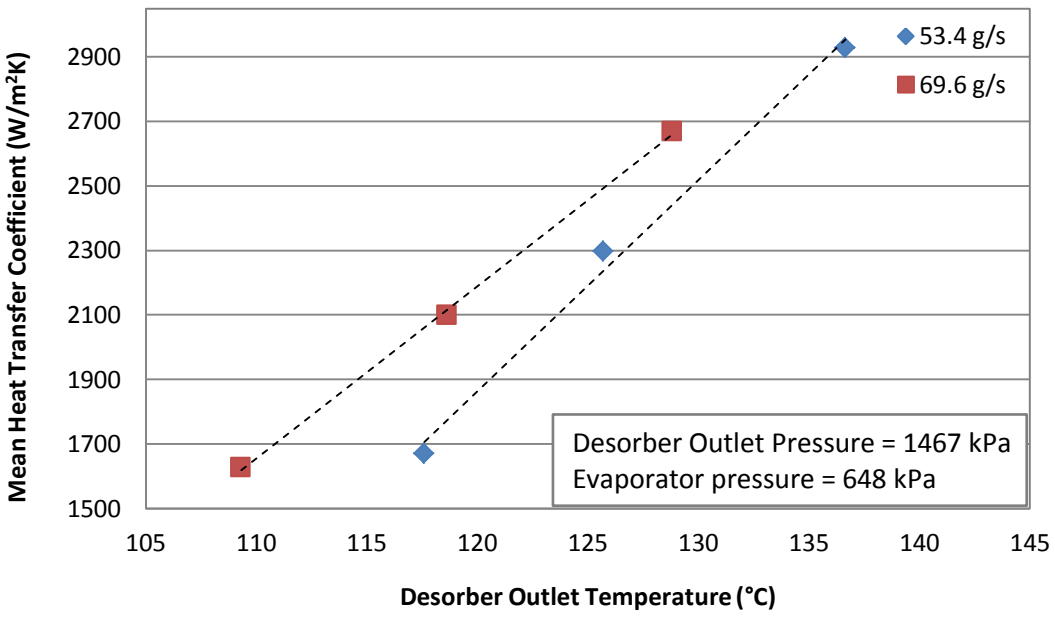

Figure 5.17: Mean Heat Transfer Coefficient as a Function of Desorber Outlet Temperature at Constant Pressure

5.2.2. Desorber Quality Effect

The effect of an increasing desorber entrance quality on the mean heat transfer coefficient is visualized in Figure 5.18. Higher solution temperatures enhance heat and mass transfer throughout the system, including the solution heat exchanger, reflected in an increasing desorber entrance quality along a higher mean heat transfer coefficient. Higher poor solution mass flow rates also enhance heat and mass transfer, therefore an equal or greater growth is expected in the entrance quality, yet lower qualities are reflected in Figure 5.18.

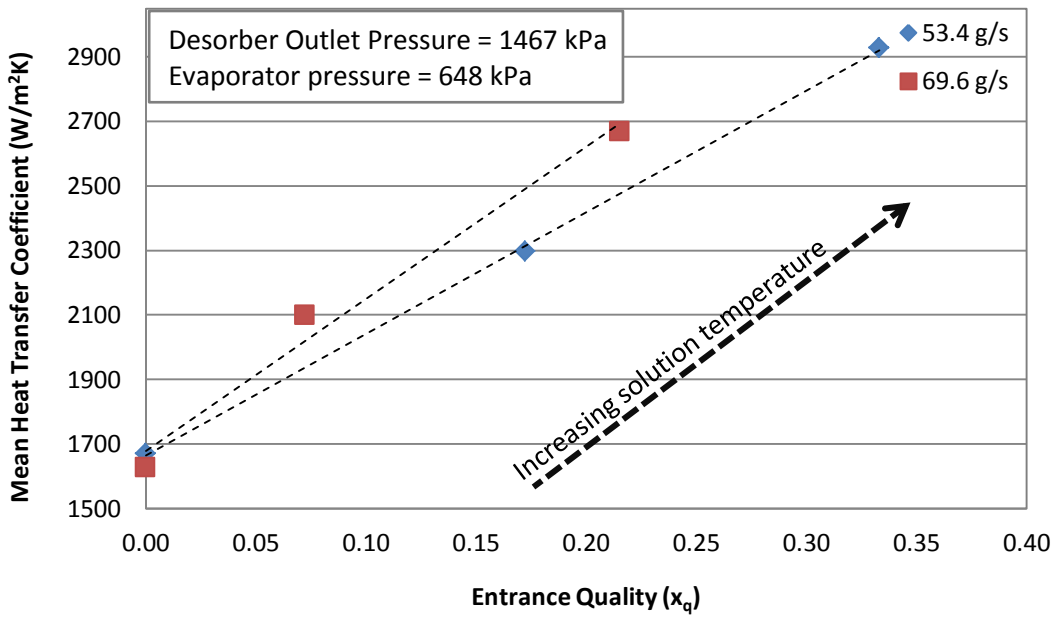

Figure 5.18: Mean Heat Transfer Coefficient as a Function of Desorber Entrance Quality at Constant Pressure

This reversed trend alone can be a product of lower desorber inlet temperatures at higher mass flow rates. Therefore, to further investigate the trend, the quality difference across the desorber was studied as a percentage function of maximum possible quality difference based on the desorber inlet quality, poor solution liquid concentration and rich solution liquid concentration (Equation 48, Equation 49) (Figure 5.19).

$$\%\Delta x_{q,des} = 100\left(\frac{x_{q,out} - x_{q,in}}{x_{q,max} - x_{q,in}}\right) \qquad \text{Equation 48}$$

$$x_{q,max} = 1 - \left(\frac{x_{rich\ solution}\dot{m}_{rich\ solution}}{x_{poor\ solution}\dot{m}_{poor\ solution}}\right) \qquad \text{Equation 49}$$

A 53.4 g/s solution mass flow rate reflects a reversal of the expected trend of an increasing quality difference across the desorber as the solution temperature increases. The reversed quality difference decrease occurs once more as the solution

mass flow rate is increased. On the other hand, the 69.6 g/s solution mass flow rate begins to reflect the expected trend as the quality difference across the desorber slightly increases, but then the reversal occurs and it decreases as the solution temperature increases. This is a two-fold reverse trend, first with a lower quality difference across the desorber with higher poor solution mass flow rates and second with the decrease in quality difference with higher solution temperatures. The first reverse trend is assumed to be in direct relation to the absorber performance limitation of decreasing the poor solution refrigerant concentration at higher flow rates; even though higher flow rates should increase heat and mass transfer (Figure 5.20). The second reverse trend can be a result of possible desorber dry-out, though that cannot be confirmed or denied until the absorber limitation is addressed.

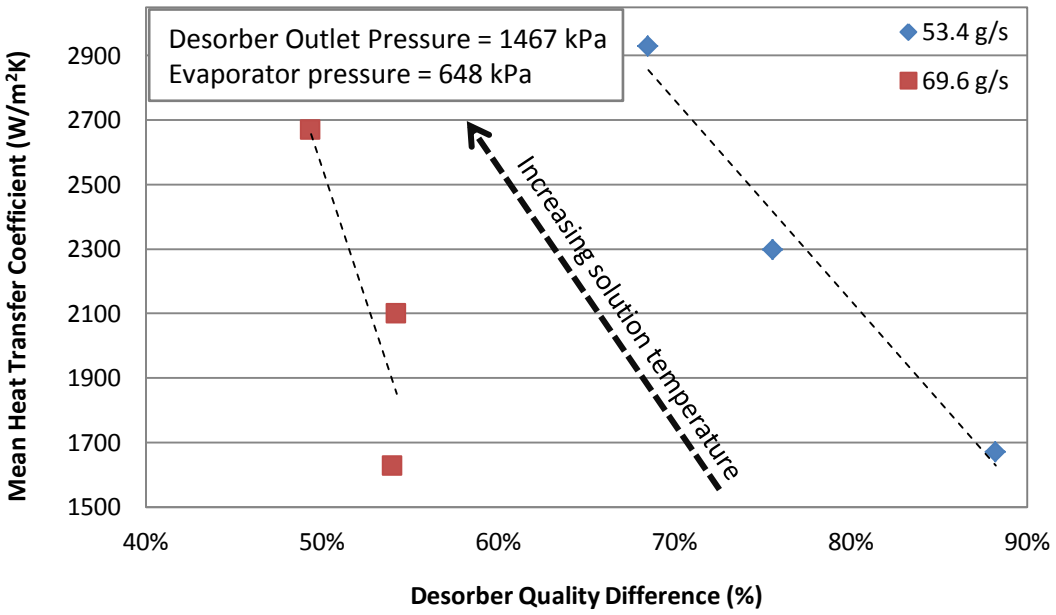

Figure 5.19: Mean Heat Transfer Coefficient as a Function of Possible Quality Difference Percentage in the Desorber at Constant Pressure

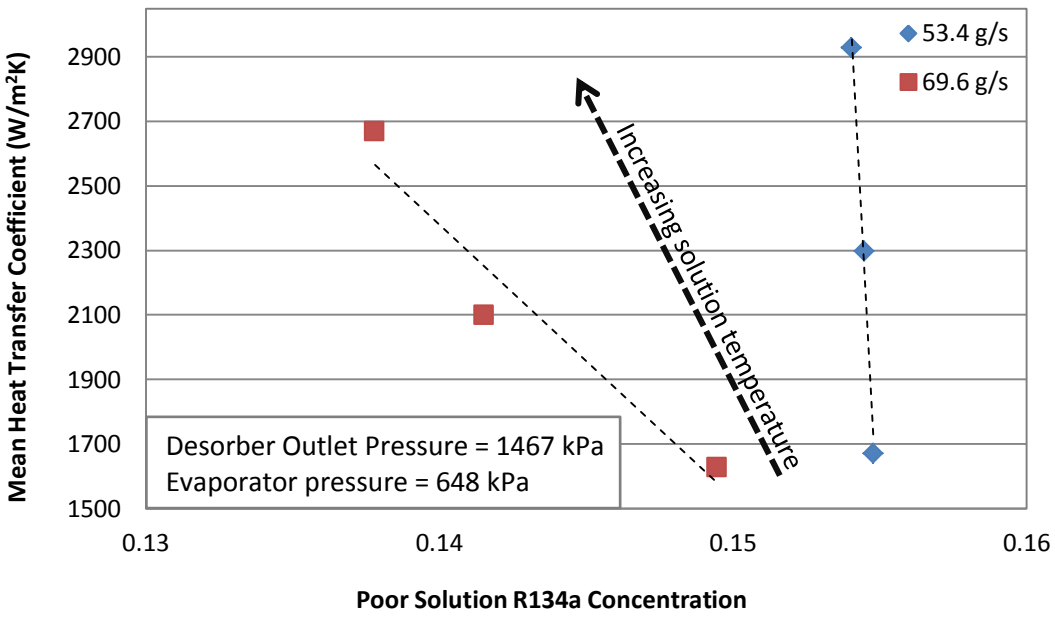

Figure 5.20: Mean Heat Transfer Coefficient as a Function of Poor Solution R134a Concentration at Constant Pressure

5.3. Absorber Mixing Visualization

Absorber mixing visualization was achieved by placing a sight glass at the exit of the pre-absorber mixing chamber; directly after the R134a/rich solution streams mix and enter the absorber heat exchanger (Figure 2.3 and Figure 2.13). Mixing visualization was desired to confirm the effectiveness of the sparger mixing chamber design. A video camera was placed above the mixing sight glass and pictures were taken throughout system runs to examine the mixing effect. It was observed that the effective mixing threshold was around 4 g/s vapor generation. Poor to no mixing, below the threshold, reflected a liquid flow with one main vapor bubble (Figure 5.21 - Left). Good mixing began with the formation of small bubbles foaming and flowing in a liquid stream (Figure 5.21 - Center). Excellent mixing

exhibited a jet of foaming bubbles mixing into the liquid stream as it flows through (Figure 5.21 - Right).

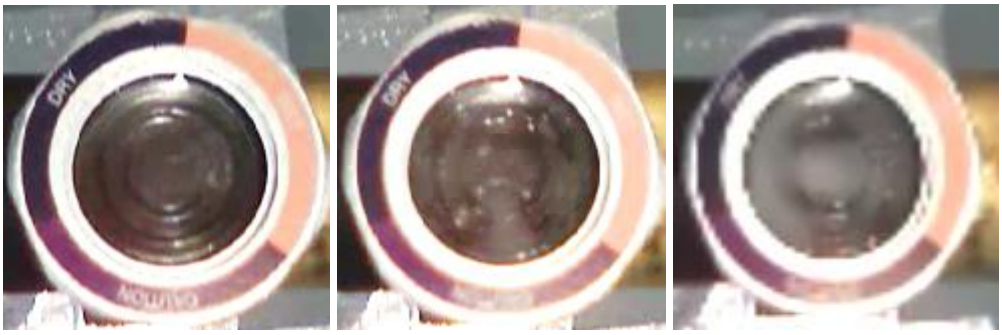

Figure 5.21: Absorber Mixing Sight Glass

At higher vapor generation rates, above 4 g/s, the vapor flow has enough force to push through the sparger and get carried away with the assistance of the liquid stream as it flows over the sparger walls, before reforming into a larger vapor bubble. At some point, around 6 g/s, the vapor flow has enough force to push through the sparger with or without the assistance of the liquid stream. At this point it appears that the generalized, above 4 g/s, phenomena is still occurring while an additional jet of vapor bubbles forces its way through the front of the sparger. The occurrence of good mixing at higher vapor flow rates is of no surprise, as the pre-mixing chamber was designed with the higher expected vapor generation flow rates in mind.

5.4. Working Fluid Concentration Sample Testing

Equilibrium concentration data verification was achieved through poor and rich solution sampling. Sampling ports were built into the system on both rich and poor solution sides (Figure 2.3). Sampling was conducted based on ASHRAE standard 41.4 and was completed by following the procedure laid out in section 3.4 [43]. Equilibrium concentration data verification was desired for comparison with

dynamic system data and see how it differs. In addition, verification of data matching between equilibrium and dynamic data was desired in order to validate the use of equilibrium concentration values during system analysis. A sample test was taken and compared against its CHEMCAD values (Table 7). The poor solution was found to have a close agreement, 3% relative error, between the sample and CHEMCAD value, while the rich solution was found to have a larger relative error of 12%. The larger rich solution deviation was assumed to be the result of a smaller R134a concentration value, therefore making equal mass uncertainty have a greater relative impact on the value agreement. The close agreement of the poor solution concentration gave legitimacy to the use of CHEMCAD concentration values in various calculations.

Table 7: Sample Testing

	Sample	CHEMCAD
Poor solution	15.6%	15.1%
Rich solution	5.75%	6.54%

Chapter 6: Conclusions and Future Work

A single-effect absorption facility was designed and constructed to investigate the performance of a 3 kW capacity mini-channel desorber in an off-grid high temperature application, while utilizing an R134a/POE32 solution mixture. The desorber was designed to replicate the utilization of waste heat from a generator source. The absorber was designed to be air-cooled at 35°C ambient conditions. The experimental facility was comprised of a solution loop, refrigerant loop, water loop and wind tunnel. Test run combinations were performed over a 120 to 150°C desorption temperature range, a 1,333 to 1,614 kPa desorption pressure range, 53.4 to 69.9 g/s poor solution mass flow rates and over a 19.2 to 23.3% system refrigerant concentration.

Desorption performance, combination of desorber and post-heater, was evaluated based on the variation of system parameters and the resulting vapor generation, circulation ratio and poor solution concentration. Expected data trends of increasing vapor generation and decreasing circulation ratio were observed as a result of increasing solution temperatures, decreasing desorption pressures and increasing system refrigerant concentrations. Reversed data trends of decreasing poor solution concentration and therefore increasing circulation ratio were observed as a result of increasing poor solution mass flow rates, while an expected increasing vapor generation was observed. These trend reversals were concluded as linked directly to poor absorber performance due to observed pressure, temperature and solubility limitations. Further investigation of absorber performance limitations should be pursued to examine the source of the limitation, whether it is absorber design or

mixture solubility. The highest vapor generation rate of 7.34 g/s was achieved at a 9.54 circulation ratio, 16% poor solution concentration, desorption temperature and pressure of 150°C and 1,353 kPa, 69.9 g/s poor solution mass flow rate and a 23.3% system refrigerant concentration.

Desorber performance was further evaluated based on mean heat transfer coefficient and quality difference, as a percent of maximum possible, across the desorber. Mean heat transfer coefficient calculations were conducted using a fin efficiency model. Quality values were obtained by utilizing CHEMCAD's equilibrium data based EOS calculations as functions of measured temperatures and pressures. Expected data trends of increasing mean heat transfer coefficient were observed as a result of increasing solution temperatures, decreasing desorption pressures and increasing poor solution mass flow rates. Reversed data trend of decreasing quality difference was observed as a result of increasing poor solution mass flow rates and increasing solution temperatures. This trend was once again concluded as linked directly to poor absorber performance due to observed pressure, temperature and solubility limitations. In addition, at the 69.6 g/s poor solution mass flow rate, a minimal increase in quality difference across the desorber quickly reversed and decreased as a result of increasing solution temperatures. This trend reversal was hypothesized as a result of desorber dry-out, though denial/affirmation cannot be established until absorber limitations are further explored. The highest mean heat transfer coefficient of 3,456 W/m^2K was achieved at a 60% possible quality difference, 7.5 circulation ratio, 18% poor solution concentration, desorption

temperature and pressure of 151°C and 1,229 kPa, 53.5 g/s poor solution mass flow rate and a 23.3% system refrigerant concentration.

The results of this investigation contribute mini-channel desorber testing data in a dynamic testing configuration while utilizing an R134a/POE32 solution mixture. The results will be utilized for desorber and absorber design improvements in preparation for further testing. The modified desorber and absorber will then be utilized in the final design and construction of a full scale 17.6 kW (5 ton) hybrid absorption vapor compression system in an off-grid high temperature location.

Finally, the desorber exhibited all the promising heat transfer enhancements associated with mini-channel heat exchanger design, while showing adverse mass transfer performance that, at the present point, is associated with poor absorber performance. The conclusions of this investigation highlight the need for further absorber modification and testing as part of future work.

Taking into account the observed absorber limitations during this experimental investigation, further absorber modifications are necessary to create a successful hybrid absorber vapor compression system. One possible improvement modification would be to reposition the compressor. Hybrid absorber vapor compression systems come in many configurations. The current configuration places the electric compressor in parallel with the ABS to share the cooling load with a parallel VCS. The suggested change would be to reposition the compressor and place it in-line between the evaporator and absorber (Figure 6.1). In this position the compressor gives a low pressure lift between the evaporator and absorber, allowing the evaporator to run at lower pressures than the absorber. The lower evaporator

pressure helps provide the desired cooling capacity at the specified conditioned space parameters. The low pressure lift provides the absorber a higher working pressure. Absorption occurs more readily at higher pressures. Therefore, higher poor solution concentrations can be achieved at the same working temperatures, leading to higher desorption rates and lower desired circulation ratios.

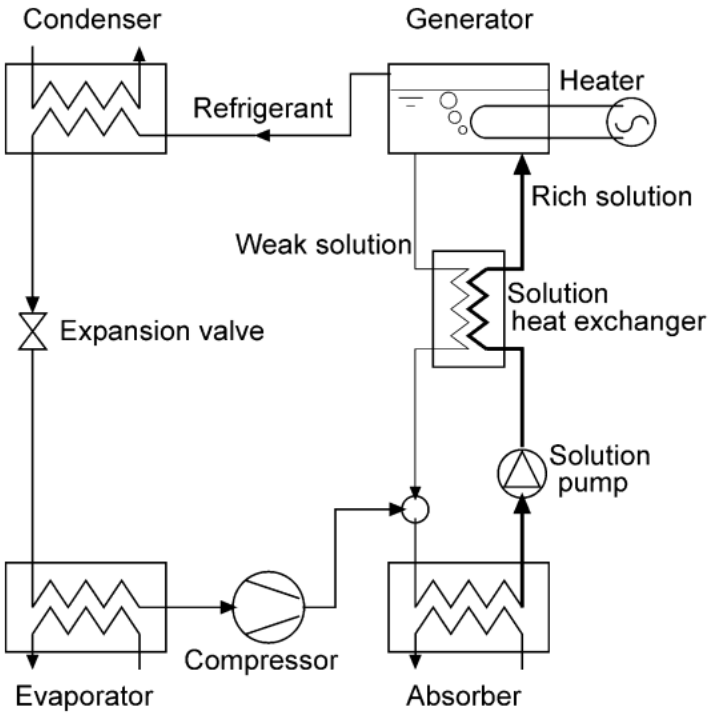

Figure 6.1: Alternative Hybrid Absorption Vapor Compression System Configuration [13]

At lower poor solution mass flow rates the desorber exhibited good heat transfer properties. If possible mini-channel desorber dry-out still presents itself in new data, once absorber modifications are completed and proven successful, a wider channel width shim, with less channels, can be created and utilized in the same desorber set-up.

Single component testing for the desorber, in order to by-pass absorber limitations, is also a possibility that can be explored. This option has been previously conducted at lower system temperatures and pressures [50], but its limitation is inherent in component isolation. Isolated single component testing will not account for changing R134a/POE32 solution mixture properties under dynamic system testing. Therefore, if the absorber is presenting as the limiting component, final desorber conclusions must be made only after dynamic system testing such as this investigation. Another way this could be accomplished would be to run the current system and use the evaporator as a second condenser, leading to liquid mixing in the absorber. This would theoretically by-pass the absorption limitations on the absorber end while still maintaining the importance of dynamic system testing.

References

1. Astbury, R. *World Energy Consumption*. 2010; Available from: http://www.thephysicist.co.uk/2010/11/world-energy-consumption/.
2. EIA, *International Energy Statistics: Total Primary Energy Consumption*. 2012, U.S. Energy Information Administration.
3. EIA. *EIA projects world energy consumption will increase 56% by 2040*. 2013; Available from: http://www.eia.gov/todayinenergy/detail.cfm?id=12251.
4. CDIAC, *Recent Greenhouse Gas Concentrations*. 2013, Carbon Dioxide Information Analysis Center (CDIAC).
5. EIA, *How much energy is consumed in residential and commercial buildings in the United States*. 2012, U.S. Energy Information Administration.
6. DOE, *Energy Efficiency Trends in Residential and Commercial Buildings*. 2010, U.S. Department of Energy.
7. Pérez-Lombard, L., J. Ortiz, and C. Pout, *A review on buildings energy consumption information.* Energy and Buildings, 2008. **40**(3): p. 394-398.
8. IEA, *CHP and District Cooling: An Assessment of Market and Policy Potential in India*. 2010, International Energy Agency (IEA).
9. Herold, K.E., R. Radermacher, and S.A. Klein, *Absorption Chillers and Heat Pumps*. 1996, Boca Raton, FL: CRC Press.
10. EIA, *Average Tested Heat Rates by Prime Mover and Energy Source, 2007-2011*. 2012, U.S. Energy Information Administration.

11. Ayala, R., C.L. Heard, and F.A. Holland, *Ammonia/lithium nitrate absorption/compression refrigeration cycle. Part II. experimental.* Applied Thermal Engineering, 1998. **18**(8): p. 661-670.

12. Ventas, R., et al., *Ammonia-lithium nitrate absorption chiller with an integrated low-pressure compression booster cycle for low driving temperatures.* Applied Thermal Engineering, 2010. **30**(11–12): p. 1351-1359.

13. Fukuta, M., et al., *Performance of compression/absorption hybrid refrigeration cycle with propane/mineral oil combination.* International Journal of Refrigeration, 2002. **25**(7): p. 907-915.

14. Kulkarni, D.P., et al., *Application of aluminum oxide nanofluids in diesel electric generator as jacket water coolant.* Applied Thermal Engineering, 2008. **28**(14–15): p. 1774-1781.

15. Haidar, J.G. and J.I. Ghojel. *Waste heat recovery from the exhaust of low-power diesel engine using thermoelectric generators*. in *Thermoelectrics, 2001. Proceedings ICT 2001. International Conference on*. 2001.

16. Taymaz, I., *An experimental study of energy balance in low heat rejection diesel engine.* Energy, 2006. **31**(2–3): p. 364-371.

17. Wang, T., et al., *A review of researches on thermal exhaust heat recovery with Rankine cycle.* Renewable and Sustainable Energy Reviews, 2011. **15**(6): p. 2862-2871.

18. Killion, J.D. and S. Garimella, *A critical review of models of coupled heat and mass transfer in falling-film absorption.* International Journal of Refrigeration, 2001. **24**(8): p. 755-797.

19. Castro, J., et al., *Comparison of the performance of falling film and bubble absorbers for air-cooled absorption systems.* International Journal of Thermal Sciences, 2009. **48**(7): p. 1355-1366.

20. de Vega, M., J.A. Almendros-Ibañez, and G. Ruiz, *Performance of a LiBr–water absorption chiller operating with plate heat exchangers.* Energy Conversion and Management, 2006. **47**(18–19): p. 3393-3407.

21. Táboas, F., et al., *Flow boiling heat transfer of ammonia/water mixture in a plate heat exchanger.* International Journal of Refrigeration, 2010. **33**(4): p. 695-705.

22. García-Hernando, N., et al., *On the pressure drop in Plate Heat Exchangers used as desorbers in absorption chillers.* Energy Conversion and Management, 2011. **52**(2): p. 1520-1525.

23. Annamalai, M. and B. Pasupathy, *Effect Of Operational Parameters On Heat and Mass Transfer In Generator of R134a/DMF Absorption Refrigeration System*, in *International Refrigeration and Air Conditioning Conference*. 2012.

24. Balamurugan, P. and A. Mani, *Experimental studies on heat and mass transfer in tubular generator for R134a-DMF absorption refrigeration system.* International Journal of Thermal Sciences, 2012. **61**(0): p. 118-128.

25. Field, B.S. and P. Hrnjak, *Pressure Drop of Two-Phase Refrigerant-Oil Mixtures in a Small Channel*, in *International Refrigeration and Air Conditioning Conference*. 2006.

26. Harirchian, T. and S.V. Garimella, *Effects of Channel Dimension, Heat Flux , and Mass Flux on Flow Boiling Regimes in Microchannels*. 2009: Cooling Technologies Research Center.

27. Bowers, M.B. and I. Mudawar, *High flux boiling in low flow rate, low pressure drop mini-channel and micro-channel heat sinks.* International Journal of Heat and Mass Transfer, 1994. **37**(2): p. 321-332.

28. Nino, V.G., P.S. Hrnjak, and T.A. Newell, *Characterization of Two- Phase Flow in Microchannels*. 2002, Air Conditioning and Refrigeration Center.

29. Cavallini, A., et al., *Two-phase frictional pressure gradient of R236ea, R134a and R410A inside multi-port mini-channels.* Experimental Thermal and Fluid Science, 2005. **29**(7): p. 861-870.

30. Determan, M.D. and S. Garimella, *Ammonia–water desorption heat and mass transfer in microchannel devices.* International Journal of Refrigeration, 2011. **34**(5): p. 1197-1208.

31. Zhang, W., T. Hibiki, and K. Mishima, *Correlations of two-phase frictional pressure drop and void fraction in mini-channel.* International Journal of Heat and Mass Transfer, 2010. **53**(1–3): p. 453-465.

32. Murphy, K.P. and B.A. Phillips, *Development of a residential gas absorption heat pump.* International Journal of Refrigeration, 1984. **7**(1): p. 56-58.

33. Fatouh, M. and M.S. Srinivasa, *Comparison of R22-absorbent pairs for absorption cooling based on P-T-X data.* Renewable Energy, 1993. **3**(1): p. 31-37.

34. Sujatha, K.S., A. Mani, and S.S. Murthy, *Analysis of a bubble absorber working with R22 and five organic absorbents.* Heat and Mass Transfer, 1997. **32**(4): p. 255-259.

35. Borde, I., M. Jelinek, and N.C. Daltrophe, *Working fluids for an absorption system based on R124 (2-chloro-1,1,1,2,-tetrafluoroethane) and organic absorbents.* International Journal of Refrigeration, 1997. **20**(4): p. 256-266.

36. Borde, I., M. Jelinek, and N.C. Daltrophe, *Absorption system based on the refrigerant R134a.* International Journal of Refrigeration, 1995. **18**(6): p. 387-394.

37. Wahlström, Å. and L. Vamling, *Solubility of HFC32, HFC125, HFC134a, HFC143a, and HFC152a in a Pentaerythritol Tetrapentanoate Ester.* Journal of Chemical & Engineering Data, 1999. **44**(4): p. 823-828.

38. Wahlström, Å. and L. Vamling, *Solubility of HFCs in Pentaerythritol Tetraalkyl Esters.* Journal of Chemical & Engineering Data, 1999. **45**(1): p. 97-103.

39. Marsh, K.N. and M.E. Kandil, *Review of thermodynamic properties of refrigerants + lubricant oils.* Fluid Phase Equilibria, 2002. **199**(1–2): p. 319-334.

40. Yokozeki, A., *Theoretical performances of various refrigerant–absorbent pairs in a vapor-absorption refrigeration cycle by the use of equations of state.* Applied Energy, 2005. **80**(4): p. 383-399.

41. Mainstream Engineering Corporation., *Personal Communication*.

42. *ANSI/ASHRAE Standard 55-2010: Thermal Environmental Conditions for Human Occupancy*. 2010, American Society of Heating, Refrigeration and Air-Conditioning Engineers (ASHRAE).

43. *ANSI/ASHRAE Standard 41.4-1996: Method for Measurement of Proportion of Lubricant in Liquid Refrigerant*. 1996, American Society of Heating, Refrigeration and Air-Conditioning Engineers (ASHRAE).

44. *ASHRAE Standard 41.2-1987 (RA92): Standard Methods for Laboratory Air-Flow Measurement* 1987, American Society of Heating, Refrigeration and Air-Conditioning Engineers (ASHRAE).

45. Youbi-Idrissi, M., et al., *Impact of refrigerant–oil solubility on an evaporator performances working with R-407C.* International Journal of Refrigeration, 2003. **26**(3): p. 284-292.

46. *XProps 2.0*. 2010, Optimized Thermal Systems LLC.

47. *ANSI/ASHRAE Standard 37-2009: Methods of Testing for Rating Electrically Driven Unitary Air-Conditioning and Heat Pump Equipment*. 2009, American Society of Heating, Refrigeration and Air-Conditioning Engineers (ASHRAE).

48. *AProp*. 2012, Center for Environmental Energy Engineering: University of Maryland.

49. *REFPROP 8.0*. 2010, National Institute of Standards and Technology.

50. Field, B.S. and P. Hrnjak, *Two-Phase Pressure Drop and Flow Regime of Refrigerants and Refrigerant-Oil Mixtures in Small Channels*. 2007: Air Conditioning and Refrigeration Center.

51. Qu, W. and I. Mudawar, *Flow boiling heat transfer in two-phase micro-channel heat sinks—I. Experimental investigation and assessment of correlation methods.* International Journal of Heat and Mass Transfer, 2003. **46**(15): p. 2755-2771.